aerospace

MDPI

Article

Aerospike Aerodynamic Characterization at Varying Ambient Pressures

Luca Fadigati [1,*], Marco Daniel Gagliardi [1], Ernesto Sozio [2], Federico Rossi [3], Nabil Souhair [3] and Fabrizio Ponti [1]

[1] Department of Industrial Engineering, University of Bologna, Via Zamboni, 33-40126 Bologna, Italy; marco.gagliardi2@studio.unibo.it (M.D.G.); fabrizio.ponti@unibo.it (F.P.)
[2] Pangea Propulsion, Av. Numero uno, 20-08040 Barcelona, Spain; ernesto.sozio@pangeapropulsion.com
[3] Aerospace and Automotive Engineering School, International University of Rabat, Shore Rocade, Rocade S, Rabat 11103, Morocco; federico.rossi@pangeapropulsion.com (F.R.); nabil.souhair@uir.ac.ma (N.S.)
* Correspondence: luca.fadigati@studio.unibo.it

Abstract

Due to the recent improvement in the additive manufacturing field, aerospike engines have been reconsidered as a possible alternative to the traditional bell-shaped nozzles. The former offer higher thrust and specific impulse during the launcher ascension phase because they are theoretically able to adapt the gas expansion ratio, reaching the optimal condition for a wide range of ambient pressure values, while bell-shaped nozzles can achieve the optimal expansion condition only at the design altitude. This capability has been proved for full-length plug nozzles, which, however, have some drawbacks, like a low thrust-to-weight ratio and challenging design of the cooling system at the spike tip. Therefore, research is moving towards truncated spike geometries, which allow the previously mentioned issues to be overcome. The aim of this work is to verify the expansion adaptation ability of a specific truncated aerospike geometry at different ambient pressures and to develop a simplified theory to estimate the upper bound of the base thrust coefficient. The analysis has been addressed by running numerical fluid dynamics simulations performed with an OpenFOAM solver.

Keywords: aerospike; compressible supersonic flow; shape optimization; Prandtl–Meyer expansion; launcher ascension

1. Introduction

Several designs, alternative to the traditional bell-shaped nozzles, have been proposed since the 1960s [1]. One of them is the plug nozzle, the main advantage of which is the ability to work in the optimal expansion condition for a wide range of ambient pressure values, theoretically reaching the highest possible thrust coefficient and specific impulse during the launcher ascension. The bell-shaped nozzle, instead, works in the optimal expansion condition only at one ambient pressure [2–4]. Hence, it operates most of the time in off-design conditions. According to [5] (p. 84), the plug nozzle is able to work near optimal performance at every altitude. Its major issue is the cooling system design. Effective plug tip cooling is particularly difficult to achieve due to the small space available. This issue is solved with the aerospike engine by truncating the plug at a given axial distance from the throat section, but with the inconvenience of possible thrust losses. Unfortunately, determining if the development of an aerospike engine could bring tangible benefits to today's launcher technology is not an easy task.

Check for updates

Academic Editor: Stephen Whitmore

Received: 3 November 2025
Revised: 14 December 2025
Accepted: 16 December 2025
Published: 24 December 2025

Nowadays, a lot of researchers are working on aerospike technology in order to improve its performance. For example, S. B. Verma, N. Gayathri, and P. P. Nair have studied the conical nozzle and the truncated conical nozzle [6–8] through experiments and numerical simulations. Liu has worked on the optimization of the design of an aerospike with rotating detonation [9]. Wang has elaborated a simplified design and optimization method for defining the aerospike nozzle contour, describing the spike with a parabola [10]. He is also working on the expansion–deflection nozzle [11,12], which works similarly to the aerospike one: the flow is expanded through a Prandtl–Meyer expansion and, therefore, it is able to adapt the expansion ratio according to the ambient pressure. The aerospike nozzle has also been studied, both numerically by Li and Huang in [13–16] and experimentally by Zhu, Z. Ma and D. Shen in [17–19], for a rotating detonation engine. In [20], Bell simulated a radial rotating detonation combustor, which expands the gas in an aerospike nozzle. In [21], Tian tested and simulated an aerospike nozzle in a hybrid rocket motor in order to improve the specific impulse and the combustion efficiency for a wider range of throttle conditions. In [22,23], Geron and Liu investigated the performance of a clustered plug nozzle in order to split the expansion between a series of traditional bell-shaped nozzles and a unique spike.

A group of researchers has been focussing on the manufacturing process of the aerospike engine. For example, Schwarzer-Fischer proposed a ceramic additive manufacturing method to build the entire thruster [24]; Pangea Aerospace [25–27] is working with Aenium [28,29] to build a low-cost additively manufactured reusable aerospike engine designed to produce a thrust in the order of 300 kN at sea level.

Despite the extensive research devoted to improving aerospike geometries, optimizing additive manufacturing processes, and characterizing their expansion behaviour under on- and off-design conditions, a systematic assessment of the adaptability of a real truncated configuration is still lacking. In particular, the literature does not fully quantify how truncation affects the ability to maintain optimal expansion over varying ambient pressures, nor does it separate the thrust contributions of the different engine surfaces. This work addresses these gaps by numerically analysing an additively manufactured aerospike demonstrator and comparing the results with simplified theoretical models. The objective is to determine under which operating conditions the truncated aerospike preserves the performance characteristics of an ideal plug nozzle and to identify the primary sources of thrust losses associated with viscous effects and geometric features such as the fillet and the truncated base.

2. Numerical Approach

The numerical methodology adopted to run the static simulations shown in this work was introduced by Fadigati in [30] and has already been used in [31–33]. Therefore, only a summary of it will be presented in this section. Among the solvers contained in the Open Field Operation And Manipulation (OpenFOAM) suite, dbnsTurbFoamhas been chosen because it has been designed to solve compressible supersonic turbulence flows. In particular, the solver uses the Harten, Lax, van Leer, Contact (HLLC) scheme described by Toro in [34], which allows capturing shock and expansion waves, achieving a sharp solution close to the discontinuities. The employed turbulence model is k-ω Shear Stress Transport (SST), which was developed by Menter [35,36]. It has been chosen because it combines the advantages of both k-ϵ and k-ω models, achieving a good solution close to and away from the walls. Due to the small engine length, a frozen expansion condition has been assumed, for which the thermodynamic and transport properties of the flow are supposed to be constant. They have been evaluated at the engine throat section, considering a complete combustion, using the software Chemical Equilibrium with Applications (CEA) [37–39], developed by National Aeronautics and Space Administration (NASA). In the following simulations, liquid oxygen and liquid methane have been considered with an oxidizer-to-fuel mass ratio of about 2.8, which is the same propellant composition adopted in [30,33]. The flow thermodynamic and transport properties are shown in Tables 1 and 2. Due to the frozen expansion condition, the flow properties shown in Tables 1 and 2 are constant in the domain; therefore, to simplify the notation, the subscript *th* (throat section) will be omitted. The CEA routine has also been used to evaluate the combustion chamber total temperature: $T_{0,\mathrm{cc}} = 3340\,\mathrm{K}$. The walls have been considered adiabatic. Every simulation has been run adjusting Δt, keeping the maximum Courant number below 0.08.

Table 1. Thermodynamic properties obtained by CEA.

Thermodynamic Properties	
p_{th} [MPa]	2.552
T_{th} [K]	3140
$C_{p_{th}}$ [J/(kg K)]	2452
γ_{th} [−]	1.206
$\mathcal{M}_{th}$ [g/mol]	19.84
ρ_{inlet} [kg/m^3]	3.1089
$c_{s_{inlet}}$ [m/s]	1272

Table 2. Transport properties obtained by CEA.

Transport Properties	
μ_{th} [kg/(m s)]	1×10^{-4}
Pr_{th} [−]	0.651
μ_{inlet} [kg/(m s)]	1×10^{-4}

3. Geometry

The simulated engine is a demonstrator additively manufactured by Pangea Aerospace. It has been designed according to Angelino's method [40] and then the spike has been truncated at about 40% of its length. This solution has been chosen to improve the cooling of the last portion of the spike and to fit the engine inside the printer, EOS M290 [41]. It has been realized in GRCop-42, which is a copper alloy developed by NASA for regeneratively cooled combustion chambers and nozzles [42,43]. The engine is axisymmetric, and it theoretically develops a thrust of about 20 kN at sea level, with a specific impulse of about 268 s. The combustion chamber nominal pressure is 45 bar (4.5 MPa).

4. Simulation Settings

4.1. Domain Size

The domain size has been decided according to the literature [8,44–46], as also discussed in [30]. To reduce the computational cost, 2D axisymmetric simulations have been run. Figure 1 shows the domain size and the boundary names. It is convenient to define a normalized curvilinear coordinate s that starts from the inlet (at which $s = 0$), follows the innermost wall, and reaches its maximum value ($s = 1$) at the end of the aerospike base (on the x-axis).

https://doi.org/10.3390/aerospace13010012

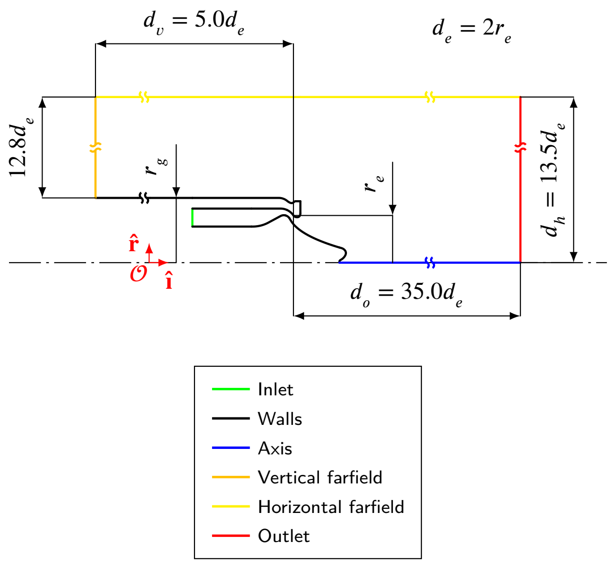

Figure 1. Domain and boundaries of the DemoP1 simulation: r_e is the engine exit section radius while r_g is the engine external wall radius. (For interpretation of the colours in the figure(s), the reader is referred to the web version of this article.)

4.2. Mesh

Figure 2 highlights the mesh in the region close to the throat section. Inside the combustion chamber and the converging nozzle, the flow direction is almost completely known from theory and, therefore, a structured mesh has been chosen; outside of it, instead, an unstructured mesh has been used because the flow there is characterized by more complex patterns. The flow boundary layer has been captured thanks to a structured mesh refinement close to every wall. Due to the high Reynolds number and the small engine size, the refinement thickness has been set a priori to 0.5 mm such that the boundary layer thickness is enclosed by it. A geometrical progression increases the cell thickness along the direction perpendicular to the walls, and, a posteriori, the value of y^+ along them has been evaluated to check that it falls in the right range: $y^+ < 100$ [47] (Section 7.6.4). The size of the cells grows towards the farfields and the outlet to dissipate any vortices to avoid the undesired backflow phenomenon and to limit the total number of cells. Figure 3 shows the mesh and the refinement region located over the spike. It has been sized according to the nozzle pressure ratio (*NPR*) to avoid increasing the total number of cells, i.e., the computational time, too much. The length of the segment BW is changed in order to have a mesh refinement region slightly larger than the main flow exiting from the engine. The exit section area A_{BW} can be geometrically evaluated as $A_{\mathrm{BW}} = \pi\left(r_{\mathrm{W}}^2 - r_B^2\right)$. It can also be estimated using Equations (1)–(3) and supposing that the pressure at the end of the spike is equal to the ambient one (This hypothesis is supported by the fact that the aerospike can work in the optimal expansion condition for a wide range of ambient pressures; hence, at the end of the spike the pressure should be equal to the ambient pressure.).

$$\frac{p_{amb}}{p_{0,\mathrm{cc}}} = \left(1 + \frac{\gamma - 1}{2} M_{\mathrm{BW}}^2\right)^{\frac{\gamma}{1-\gamma}} \tag{1}$$

$$M_{\mathrm{BW}} = \sqrt{\frac{2}{\gamma - 1}\left[\left(\frac{p_{amb}}{p_{0,\mathrm{cc}}}\right)^{\frac{1-\gamma}{\gamma}} - 1\right]} \tag{2}$$

$$A_{\mathrm{BW}} = A_{th}\frac{1}{M_{\mathrm{BW}}}\sqrt{\left[\frac{1+\frac{\gamma-1}{2}M_{\mathrm{BW}}^2}{\frac{\gamma+1}{2}}\right]^{\frac{\gamma+1}{\gamma-1}}} \tag{3}$$

The length of the segment BW can be obtained by the following equation:

$$c_{sf}A_{\mathrm{BW}} = \pi\left(r_{\mathrm{W}}^2 - r_{\mathrm{B}}^2\right) \tag{4}$$

where r_{B} and r_{W} are, respectively, the radial coordinates of the points B and W. c_{sf} is a safety factor greater than 1 that allows us to overestimate the exit section area and be sure that the refinement region ends above the shear layer. It is important that the refinement regions ends above the shear layer because, otherwise, a coarse mesh would lead to a thick shear layer with a very smooth transition between the jet flow and the flow outside. This can cause inaccuracies in the solution, like an attenuation of the shock wave reflection at the shear layer or an increase in the mass flow entrainment in the aerospike plume. The mesh close to the line JL has been sized in order to capture the thin shear layer that starts from the wall and propagates towards the outlet. In this region, a too coarse mesh would lead to a thick shear layer with a very smooth transition between the jet flow and the flow outside. The overall mesh refinement level has been chosen by performing a mesh sensitivity study, reported in Appendix A. The line CJ is the throat segment and identifies the minimum distance between the two walls. Point B has been selected at the spike end. r_e is the design exit section radius and is equal to r_{J}. However, the real value of r_e is slightly smaller than r_{J} due to the fillet between points J and L. The round connection between them is essential due to additive manufacturing technical limitations and to avoid having a sharp edge that would be difficult to cool.

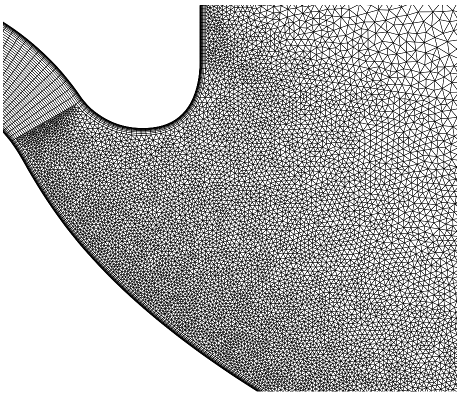

Figure 2. Magnification of DemoP1 mesh in the throat section.

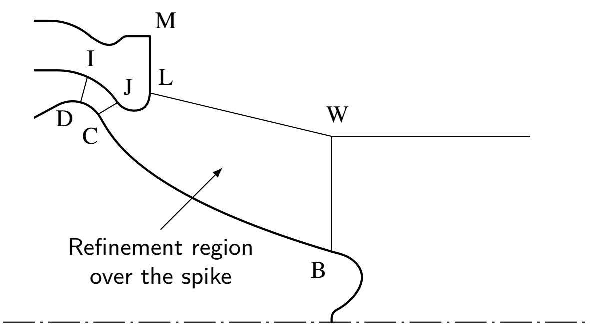

Figure 3. Magnification of the refinement region above the spike. The thick lines are the domain boundaries while the thinner ones delimit the mesh blocks. CJ is the throat section, JL is the curve segment called fillet, B has been considered the start of the base.

4.3. Boundary and Initial Conditions

Boundary conditions are defined following the nomenclature used in Figure 1. Since they are similar to those described by Fadigati in [30], only a summary will be given in this section.

- Inlet: The total pressure at the inlet linearly increases from the ambient pressure to the working conditions (4.5 MPa) in the first 33 ms. The temperature rises smoothly, reaching the combustion chamber value of 3340 K. If the flow moves into the domain, the velocity adapts according to the pressure difference between the inlet and the cell centre that has a face belonging to this boundary, while, otherwise, a zero gradient condition is imposed. ω and k have been obtained using Equations (5)–(9).

$$k_{inlet} = \frac{3}{2}(U_{inlet}\, I_{inlet})^2 \tag{5}$$

$$\omega_{inlet} = \frac{\sqrt{k_{inlet}}}{C_\mu l_{inlet}} \tag{6}$$

$$l_{inlet} = 0.07 L_{inlet} \tag{7}$$

$$I_{inlet} = 0.16 \frac{1}{Re_{D_{H_{inlet}}}^{1/8}} \tag{8}$$

$$Re_{D_{H_{inlet}}} = \frac{\rho_{inlet} D_{H_{inlet}} U_{inlet}}{\mu_{inlet}} \tag{9}$$

Equation (6) was introduced by Menter in [35]. Equation (7) is explained in Appendix B.2. The turbulence intensity has been estimated using the empirical law shown in [48] (its derivation is explained in Appendix B.1), $C_\mu = 0.09$ according to [35,36,49], $\mu_{inlet} = \mu_{th}$, and the characteristic length L_{inlet} has been chosen as the hydraulic diameter of the inlet $D_{H_{inlet}}$:

$$\begin{aligned} D_{H_{inlet}} &= \frac{4A_{inlet}}{\Phi_{inlet}} = \frac{4\pi(r_G^2 - r_F^2)}{2\pi(r_F + r_G)} \\ &= 2(r_G - r_F) \end{aligned} \tag{10}$$

r_F and r_G are, respectively, the internal and the external inlet radii, while Φ_{inlet} is the inlet perimeter. U_{inlet} can be estimated by solving the following equation for the inlet Mach number M_{inlet}.

$$\frac{A_{inlet}}{A_{th}} = \frac{1}{M_{inlet}} \left[\frac{1 + \frac{\gamma - 1}{2} M_{inlet}^2}{\frac{\gamma + 1}{2}} \right]^{\frac{\gamma+1}{2(\gamma-1)}} \tag{11}$$

where A_{inlet} is the inlet section area, A_{th} is the throat section area, and γ is the heat capacity ratio at the throat section.

$$U_{inlet} = c_{s_{inlet}} M_{inlet} = 192\,\mathrm{m/s} \tag{12}$$

$c_{s_{inlet}}$ is the speed of sound in the combustion chamber, and it is one of the CEA outputs.

$$k_{inlet} = 59.15\,\mathrm{m^2/s^2} \tag{13}$$

$$\omega_{inlet} = 2.259 \times 10^4\,\mathrm{s^{-1}} \tag{14}$$

- Walls: The normal pressure gradient on the wall has been set to zero. Then, a no slip condition has been applied to the velocity and the adiabatic wall condition has been set for the temperature. Turbulence specific dissipation ω and turbulent kinetic energy k have been modelled using wall functions [50]. They allow us to describe the behaviour of these two variables and to have a coarser grid resolution close to the wall as long as the first cell centre starting from it falls in the log-layer region. Otherwise, the height of these cells should be smaller than the viscous sublayer thickness, which is very small. The wall functions employed herein are reported in the OpenFOAM Guide [50]. A stepwise switch has been adopted between the inertial sublayer and the viscous one.

- Outlet: The flow velocity adapts accordingly to the pressure difference between the last cell centre close to the outlet and the pressure imposed at the outlet itself. Regarding pressure, a boundary condition that damps the wave reflection, imposing an advection velocity, has been used,

$$\frac{\partial p}{\partial t} + u_{wave}\frac{\partial p}{\partial x_n} = \frac{u_{wave}}{l_{inf}}(p_\infty - p) \tag{15}$$

where $u_{wave} = u_n + c_s$ is the advection speed, u_n is the flow velocity in the direction normal to the boundary, l_{inf} is the distance normal to the boundary at which the pressure should reach p_∞, and $\frac{\partial}{\partial x_n}$ is the partial derivative along a direction normal to the boundary. This boundary condition was introduced by Poinsot and Lele [51], and it has been used in other scientific works [45,52,53]. $l_{inf} = 300$ m has been imposed: this value is a compromise between wave reflection and the need to have the desired ambient pressure at the *outlet*. p_∞ has been set equal to p_{amb}. Regarding T, ω, and k, a zero flux has been imposed when the flow exits the domain, while they have been set to given values, respectively, T_{amb}, ω_o, and k_o, when the flow enters the domain. k_o and ω_o have been evaluated using the following formula, where the characteristic length employed to estimate the turbulence length scale is the engine external diameter: $l_o = 0.16 r_g$ [54] (ch. 3.7.1). Therefore,

$$k_o = \frac{3}{2}(U_r\, I_o)^2 \tag{16}$$

$$\omega_o = \frac{\sqrt{k_o}}{C_\mu l_o} \tag{17}$$

where U_r is the external flow speed.

- Farfields: A null flux is imposed when the flow exits the domain, while, in the opposite case, a fixed velocity is set parallel to the engine axis:

$$\mathbf{u}_f = \begin{bmatrix} U_r & 0 & 0 \end{bmatrix} \tag{18}$$

In static simulations, U_r should be equal to zero, but to avoid the presence of a totally quiescent flow and the consequent numerical issue, a small velocity is applied to have an equivalent Mach number of 0.01. For an inflow, the pressure flux is set to zero, while for an outflow the pressure is set to p_{amb}. Regarding the temperature, it is the opposite: the ambient temperature is imposed when the flow enters the domain and a temperature flux equal to zero is imposed when the flow exits it. The same boundary conditions set at the *outlet* are used for k and ω,

$$k_f = \frac{3}{2}\left(U_r\, I_f\right)^2 \tag{19}$$

$$\omega_f = \frac{\sqrt{k_f}}{C_\mu l_f} \quad (20)$$

with $l_f = 0.16 r_g$.

- lateral surface: OpenFOAM also requires a boundary condition, called *wedge*, for the lateral surfaces in order to set a 2D axisymmetric simulation.

Table 3 lists the boundary conditions used in the simulations with the OpenFOAM nomenclature. Regardless of the ambient pressure, the ambient temperature has been set as the sea level one in every simulation ($T_{amb} = 288.15$ K) because this parameter has no influence on the developed thrust. A zero velocity has been considered as the initial condition inside the engine and in the plume region, while $\mathbf{u}_f$ has been imposed in the outer portion of the domain. The pressure has been initialized equal to the ambient one in the whole domain. k and ω have been set constant and equal to their value at the *farfields* using Equations (19) and (20).

Table 3. Boundary condition table with OpenFOAM nomenclature.

Boundary Name	p	$\mathbf{u}$	T	k	ω
inlet	timeVarying TotalPressure	pressureInlet OutletVelocity	timeVarying UniformFixedValue	fixedValue	fixedValue
outlet	waveTransmissive	pressureInlet OutletVelocity	inletOutlet	inletOutlet	inletOutlet
vertical farfield	waveTransmissive	pressureInlet OutletVelocity	inletOutlet	inletOutlet	inletOutlet
horizontal farfield	waveTransmissive	pressureInlet OutletVelocity	inletOutlet	inletOutlet	inletOutlet
walls	zeroGradient	fixedValue	zeroGradient	kqRWallFunction	compressible:: omegaWallFunction
lateral surface	wedge	wedge	wedge	wedge	wedge

5. Static Simulation Results at Different Ambient Pressures

It is important to define two significant NPR values: NPR_{opt} and NPR_{B}. The first one corresponds to the nozzle pressure ratio at the design altitude, for which the Prandtl–Meyer expansion reaches the end of the uncut spike. To evaluate NPR_{opt}, the exit Mach number needs to be calculated by solving Equation (21), supposing $M_e > 1$. When dealing with DemoP1, $\epsilon_e = 5.0$.

$$\epsilon_e = \frac{A_e}{A_{th}^{geo}} = \frac{1}{M_e}\sqrt{\left[\frac{1+\frac{\gamma-1}{2}M_e^2}{\frac{\gamma+1}{2}}\right]^{\frac{\gamma+1}{\gamma-1}}} \implies M_e = 2.80 \quad (21)$$

$$NPR_{opt} = \frac{p_{0,\mathrm{cc}}}{p_{amb}^{opt}} = \left[1+\frac{\gamma-1}{2}M_e^2\right]^{\frac{\gamma}{\gamma-1}} = 31.76 \quad (22)$$

NPR_{B} is, instead, the nozzle pressure ratio for which the Prandtl–Meyer expansion reaches the end of the truncated spike, which is identified with point B in Figure 3. It could be similarly evaluated by imposing $\epsilon_{\mathrm{B}} = 3.16$ for DemoP1:

$$\epsilon_{\mathrm{B}} = \frac{\mathcal{A}_{\mathrm{B}}}{A_{th}^{geo}} = \frac{1}{M_{\mathrm{B}}}\sqrt{\left[\frac{1+\frac{\gamma-1}{2}M_{\mathrm{B}}^2}{\frac{\gamma+1}{2}}\right]^{\frac{\gamma+1}{\gamma-1}}} \implies M_{\mathrm{B}} = 2.45 \quad (23)$$

$$NPR_{\mathrm{B}} = \frac{p_{0,\mathrm{cc}}}{p_{amb}^{\mathrm{B}}} = \left[1+\frac{\gamma-1}{2}M_{\mathrm{B}}^2\right]^{\frac{\gamma}{\gamma-1}} = 16.32 \quad (24)$$

https://doi.org/10.3390/aerospace13010012

where M_B is the Mach number of the flow over the line LB and $\mathcal{A}_B = A_B \sin \xi_B$, in which ξ_B is the Mach angle along the line LB and A_B is the area of the truncated cone obtained by rotating the segment LB around the engine axis. A_{th}^{geo} is the throat section area, identified by the segment CJ in Figure 3.

5.1. Aerospike Performance

To evaluate the adaptability of the aerospike at different ambient pressures, DemoP1 has been simulated in static conditions at several *NPR* values. Since it is a prototype engine, its design has not been driven to maximize the delivered thrust. Therefore, it works in under-expansion conditions already at sea level with $NPR = 44.41$. Hence, in order to investigate the aerospike adaptability and to achieve over-expanded conditions keeping the same combustion chamber total pressure, it has been simulated at ambient pressure values higher than the sea level. According to the isentropic nozzle theory, the thrust coefficient and the specific impulse depend only on the *NPR*. Consequently, the following results could be extended to aerospike engines that work in over-expanded conditions at sea level. It has been decided to keep the combustion chamber total pressure fixed to have theoretically the same mass flow rate in every simulation. The tested *NPR* range spans from 3.21 up to 90.00. The values 16.32 and 31.76 have been included in the analysis because they correspond, respectively, to the *NPR* value at which the Prandtl–Meyer expansion fan reaches the end of the truncated spike and the value at which expansion adaptability stops. The minimum *NPR* simulated is above 1.78, which is the minimum nozzle pressure ratio to have a sonic flow at the engine throat section. Due to the fact that the obtained solutions are unsteady, before every post-processing shown in this section, the temperature, pressure, density, and velocity fields have been averaged in time within $60\,\mathrm{ms} \leq t \leq 70\,\mathrm{ms}$. This time interval has been chosen because the thrust becomes almost constant after 60 ms.

In Figure 4, the engine is working in over-expansion conditions with a value of *NPR* equal to 5.62. After the throat section, the flow expands according to the Prandtl–Meyer expansion fan [55] (p. 69). A recompression and the subsequent expansion guides the flow to the end of the spike, keeping it close to the wall [5]. Figure 5 shows the non-dimensional pressure distribution, highlighting the expansion fan and oblique shock waves. In Figures 6 and 7, featuring $NPR = 16.32$, the Prandtl–Meyer expansion terminates at the end of the spike. Covering the fan expansion for the entire spike, the flow will have the same properties over the surface of the latter at any *NPR* higher than 16.32. Figures 8 and 9 show the engine in optimal expansion conditions. Therefore, at the end of the Prandtl–Meyer expansion, the flow is almost aligned with the engine axis. Figures 10 and 11, instead, show the engine in under-expansion conditions. The Prandtl–Meyer expansion ends beyond the spike and the flow expands further downstream of the geometrical engine exit section. In Figures 4, 6, 8 and 10, an expansion fan can be noticed at the end of the spike, which deviates the flow towards the engine axis [56,57]. It is then followed by a trailing shock, realigning the flow in a direction parallel to the axis itself.

Figures 5, 7, 9 and 11 show the non-dimensional pressure distribution, highlighting the expansion fan and oblique shock waves using the logarithmic scale. The aerospike expands up to the ambient pressure; therefore the pressure does not change across the shear layer, and therefore in these figures, it is depicted by a white dashed line.

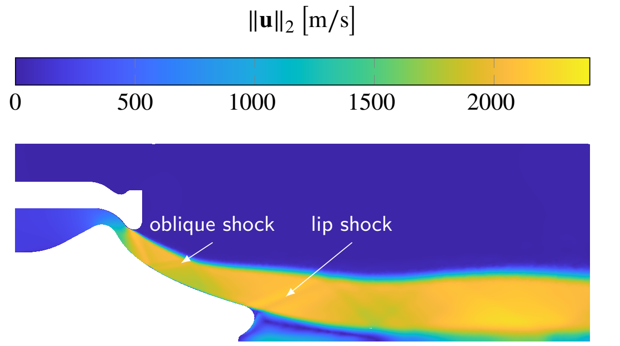

Figure 4. Velocity magnitude field of DemoP1 simulation at *NPR* = 5.62, $p_{amb}/p_{0,cc} = 0.178$ (over-expansion).

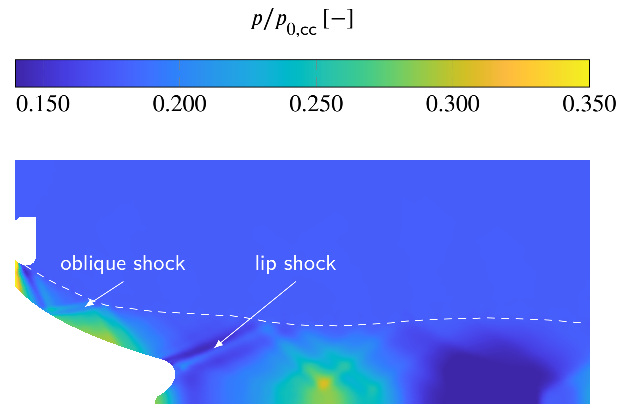

Figure 5. Non-dimensional pressure field of the DemoP1 simulation at *NPR* = 5.62, $p_{amb}/p_{0,cc} = 0.178$ (over-expansion). The shear layer is depicted by a white dashed line.

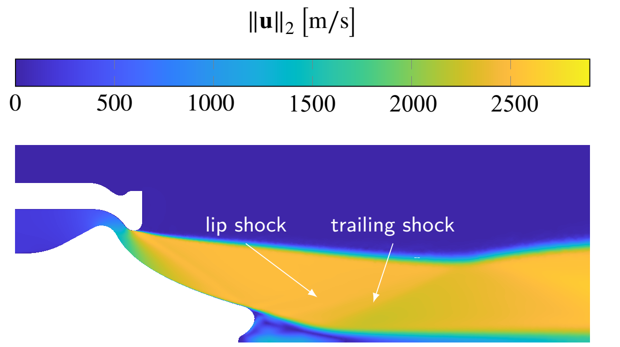

Figure 6. Non-dimensional pressure field of DemoP1 simulation at *NPR* = 16.32, $p_{amb}/p_{0,cc} = 0.061$ (over-expansion).

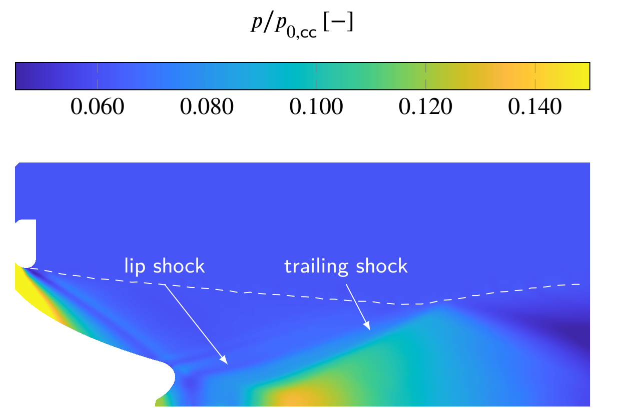

Figure 7. Velocity magnitude field of the DemoP1 simulation at *NPR* = 16.32, $p_{amb}/p_{0,cc} = 0.061$ (over-expansion). The shear layer is depicted by a white dashed line.

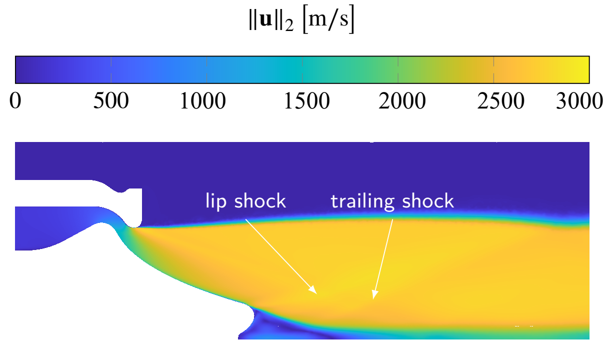

Figure 8. Velocity magnitude field of DemoP1 simulation at $NPR = 31.76$, $p_{amb}/p_{0,cc} = 0.031$ (optimal expansion).

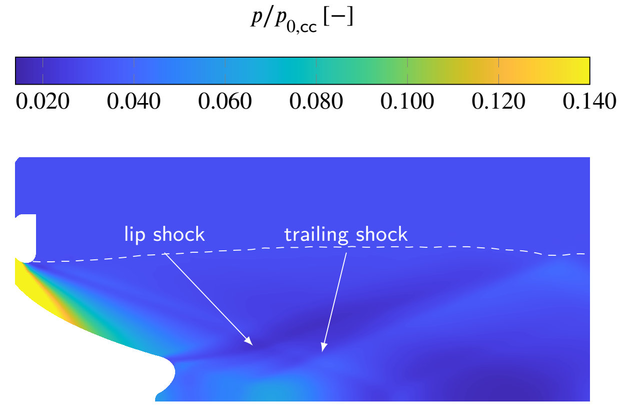

Figure 9. Non-dimensional pressure field of the DemoP1 simulation at $NPR = 31.76$, $p_{amb}/p_{0,cc} = 0.031$ (optimal expansion). The shear layer is depicted by a white dashed line.

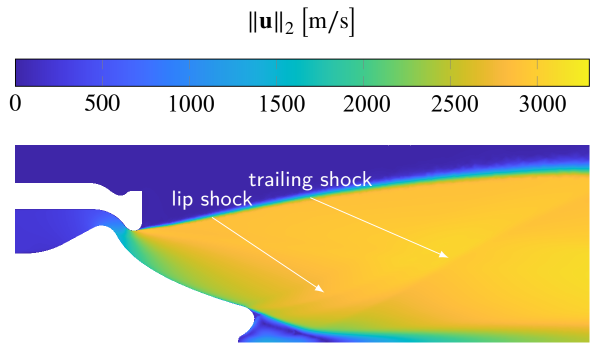

Figure 10. Velocity magnitude field of DemoP1 simulation at $NPR = 60.00$, $p_{amb}/p_{0,cc} = 0.017$ (under-expansion).

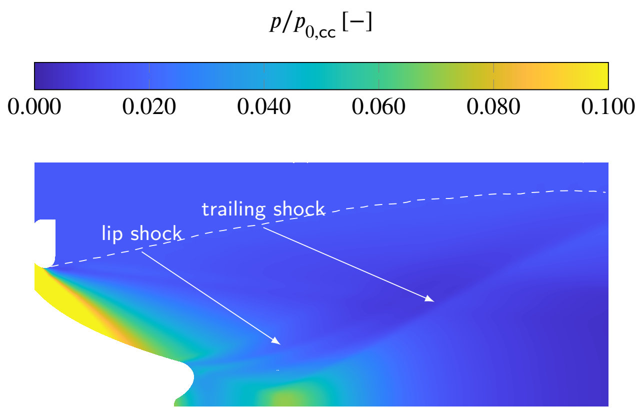

Figure 11. Non-dimensional pressure field of the DemoP1 simulation at $NPR = 60.00$, $p_{amb}/p_{0,cc} = 0.017$ (under-expansion). The shear layer is depicted by a white dashed line.

The streamline patterns shown in Figures 12–15 help interpret this behaviour. At a low NPR (Figure 12), the Prandtl–Meyer expansion covers only a portion of the spike, and the flow detaches shortly downstream of point B, forming a recirculating bubble whose size is delimited by points A and A″. As *NPR* increases, the end of the expansion fan progressively moves toward point B, as visible in Figures 13 and 14, eventually covering the entire spike at $NPR = 16.32$. This shift directly explains the trend reported for higher *NPR* values: as the expansion region increases, the thrust generated by the spike surface grows until the expansion reaches B, beyond which the pressure distribution becomes independent of ambient pressure. Figure 14 illustrates the streamline topology in optimal expansion conditions ($NPR = 31.76$). The Prandtl–Meyer fan terminates exactly at the end of the full length spike. Downstream of B, a trailing shock realigns the inner streamlines with the engine axis. In agreement with [33,57], the flow follows the spike and leaves it with an inclination that is close to its slope when the *NPR* is low, while, for high *NPR* values, only the flow, near the boundary layer, leaves the wall with an inclination that is parallel to the wall itself. Differently, away from the wall, the flow has an inclination given by the Prandtl–Meyer expansion. The recirculation bubble has a similar triangular shape in every simulation.

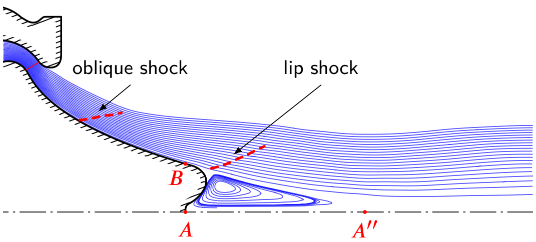

Figure 12. Streamlines of the DemoP1 simulation at $NPR = 5.62$, $p_{amb}/p_{0,cc} = 0.178$. Points A and B are, respectively, points at the base of the engine axis and the end of the spike. Meanwhile A″ highlights the end of the recirculating bubble. The throat section segment is depicted by a solid red line.

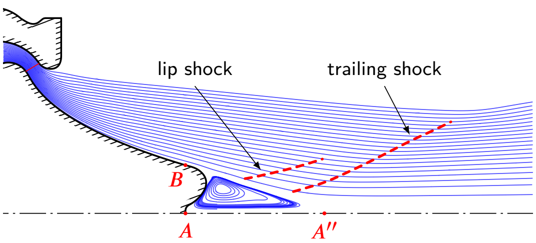

Figure 13. Streamlines of the DemoP1 simulation at $NPR = 16.32$, $p_{amb}/p_{0,cc} = 0.061$. Points A and B are, respectively, points at the base of the engine axis and the end of the spike. Meanwhile A″ highlights the end of the recirculating bubble. The throat section segment is depicted by a solid red line.

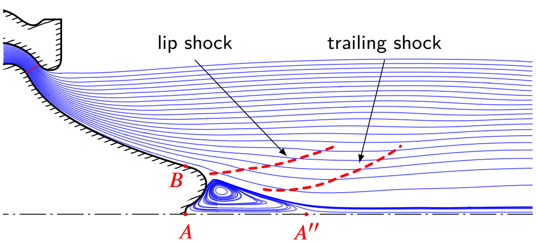

Figure 14. Streamlines of the DemoP1 simulation at $NPR = 31.76$, $p_{amb}/p_{0,cc} = 0.031$. Points A and B are, respectively, points at the base of the engine axis and the end of the spike. Meanwhile A″ highlights the end of the recirculating bubble. The throat section segment is depicted by a solid red line.

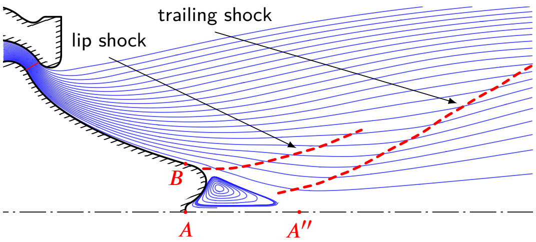

Figure 15. Streamlines of the DemoP1 simulation at $NPR = 60.00$, $p_{amb}/p_{0,\text{cc}} = 0.017$. Points A and B are, respectively, points at the base of the engine axis and the end of the spike. Meanwhile A'' highlights the end of the recirculating bubble. The throat section segment is depicted by a solid red line.

Table 4 shows the mean value of the average mass flow rate ($\underline{\dot{m}}$) evaluated in each simulation within $60\,\text{ms} \leq t \leq 70\,\text{ms}$ and its comparison with the theoretical one ($\dot{m}$). According to the isentropic nozzle theory, the mass flow rate is almost independent of the nozzle pressure ratio, but its value is lower than the theoretical one due to the boundary layer. The calculated average discharge coefficient is 0.982.

Table 4. Average DemoP1 mass flow rate compared with the theoretical one.

$\underline{\dot{m}}$ [kg/s]	$\sigma_{\underline{\dot{m}}}$ [g/s]	$\dot{m}$ [kg/s]	$\Delta\dot{m}$ [kg/s]	C_d [−]
7.695	4.174	7.838	−0.143	0.982

Figures 16 and 17 show the comparison between isentropic nozzle theory and the simulation results. The blue line outlines an ideal nozzle with a variable aspect ratio that always works in optimal expansion conditions. This line can be considered as a theoretical upper limit. The orange and yellow dashed lines represent, respectively, an ideal plug nozzle (for more detail see Appendix C) and an ideal bell-shaped nozzle that have been designed with the same aspect ratio as DemoP1. The violet dots are the thrust coefficients obtained from the simulations using the following formula:

$$\underline{C}_F = \frac{\underline{F}}{A_{th}^{geo}\, p_{0,\text{cc}}} \tag{25}$$

where A_{th}^{geo} is the geometrical throat section identified by the segment CJ in Figure 3, while the thrust $\underline{F}$ has been calculated as explained in [33]:

$$\underline{F} = \underline{F}_\text{inlet} + \underline{F}_\text{walls} \tag{26}$$

$$\underline{F}_\text{inlet} = \hat{\mathbf{n}}_{ea} \cdot \int_{S_\text{inlet}} \left[\underline{\rho}\, \underline{\mathbf{u}} (\underline{\mathbf{u}} \cdot \hat{\mathbf{n}}) + \left(\underline{p} - p_{amb} \right) \hat{\mathbf{n}} \right] dA \tag{27}$$

$$\underline{F}_\text{walls} = \hat{\mathbf{n}}_{ea} \cdot \int_{S_\text{wall}} \left[\left(\underline{p} - p_{amb} \right) \mathrm{I} + \underline{\boldsymbol{\tau}} \right] \hat{\mathbf{n}}\, dA \tag{28}$$

where $\hat{\mathbf{n}}_{ea}$ is the unit vector parallel to the engine axis, pointing toward the engine inlet, $\hat{\mathbf{n}}$ is the outward surface normal unit vector, S_inlet is the inlet surface, and S_walls is the surface obtained from the union of all the solid walls (Figure 1). $\underline{F}$ contains the wall shear stress contribution. It can be noticed that, despite the spike truncation, DemoP1 is still able to achieve a thrust coefficient close to that of the ideal plug nozzle both in the under-expanded and over-expanded conditions (violet dots in Figure 16). The thrust coefficient losses can be correlated with two-dimensional geometry and viscous losses. The thrust coefficients obtained by the simulations have also been evaluated with an equivalent throat section area calculated by inverting the formula for the isentropic nozzle mass flow rate.

$$A_{th}^{eq} = \frac{\dot{m}}{p_{0,\mathrm{cc}}}\sqrt{\frac{R_s T_{0,\mathrm{cc}}}{\gamma}}\left(\frac{\gamma+1}{2}\right)^{\frac{\gamma+1}{2(\gamma-1)}} \tag{29}$$

The use of the equivalent throat section area allows us to remove the effect of thrust reduction directly related to the reduction in mass flow rate because using A_{th}^{eq} to evaluate the thrust coefficient corresponds to comparing the simulation results with an ideal bell-shaped nozzle that has a mass flow rate equal to the one obtained from the simulation. Hence, in the case of thrust losses, they are not related to the reduction in mass flow rate, but they depend only on the pressure distribution over the engine surfaces or skin friction. The thrust coefficient values computed with the equivalent throat section are displayed in Figure 16 with green dot markers. They are almost overlapped with the curve of an ideal plug nozzle. Therefore, it is possible to assume that this aerospike is working like a non-truncated plug nozzle because the base is able to recover the thrust lost by the plug truncation. This is also confirmed by the specific impulse comparison shown in Figure 17, in which the specific impulse calculated from the simulations is almost coincident with the ideal one. The average ΔC_F between the simulated DemoP1 and the ideal plug nozzle is -2.79% of the theoretical thrust coefficient using the geometrical throat section area, while it drops to -0.98% when the equivalent one (A_{th}^{eq}) is used. This result confirms that there are some losses not related to the reduction in the mass flow rate. They will be studied in Section 5.3.2. The maximum specific impulse reduction is about -1.31%. Like the ideal plug nozzle, DemoP1 loses its adaptability feature when $p_{amb} < p_{amb}^{opt}$, where p_{amb}^{opt} is the ambient pressure at which a bell-shaped nozzle, with the same aspect ratio as DemoP1, achieves the optimal expansion condition. From the isentropic theory, p_{amb}^{opt} depends only on $\epsilon_e = \frac{A_e}{A_{th}^{geo}}$. Therefore, to extend as much as possible the pressure range at which the aerospike has an optimal expansion, the engine aspect ratio should be as great as possible (compatibly with the volume and mass of the launcher on which it would be installed). p_{amb}^{B} is the ambient pressure at which the Prandtl–Meyer expansion fan reaches the spike end. Between p_{amb}^{opt} and p_{amb}^{B}, the spike reaches the maximum expansion possible and the base recovers some thrust by expanding the flow up to the ambient pressure. From the results shown in Figure 16, the aerospike is still able to achieve a thrust coefficient close to the one of the isentropic plug nozzle also in this condition.

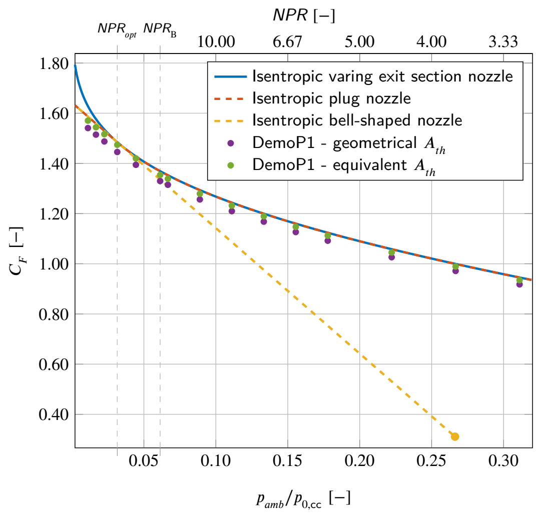

Figure 16. Thrust coefficient at different nozzle pressure ratios compared with the theoretical one.

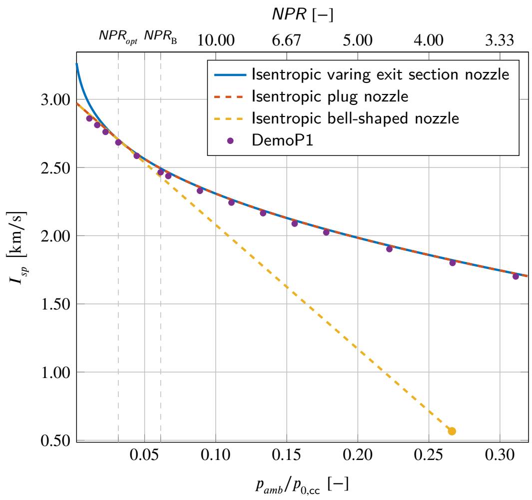

Figure 17. Specific impulse at different nozzle pressure ratios compared with the theoretical one.

5.2. Single Stage to Orbit Design

Figure 18 compares the performance of the launcher equipped with different types of engines: the blue line, which is almost completely covered by the orange dashed one, corresponds to an isentropic nozzle with a variable exit section and could be considered an upper limit for the achievable thrust coefficient; the orange dashed line corresponds to an isentropic plug nozzle with $\epsilon_e = 100$, while the yellow ones depict a family of isentropic bell-shaped nozzles obtained by varying the aspect ratio. (These lines have been obtained by applying Equations (3)–(30) [2] (p. 65)):

$$C_F = \sqrt{\frac{2\gamma^2}{\gamma - 1}\left(\frac{2}{\gamma + 1}\right)^{\frac{\gamma+1}{\gamma-1}}\left[1 - \left(\frac{p_e}{p_{0,\text{cc}}}\right)^{\frac{\gamma-1}{\gamma}}\right]} + \frac{p_e - p_{amb}}{p_{0,\text{cc}}}\epsilon_e$$

where p_e is the pressure at the exit section of the bell-shaped nozzle, and it is fixed due to the isentropic relations. The flow properties, used in the calculations, are reported in Tables 1 and 2. Let us proceed to design a Single Stage To Orbit (SSTO) launcher that has to fly from sea level up to vacuum conditions: $NPR_{sl} \to NPR_{vac}$. Assume that the engine has an expansion ratio equal to 100, while the other parameters are the same as those of DemoP1 ($p_{0,\text{cc}} = 4.5\,\text{MPa}$, $T_{0,\text{cc}} = 3340\,\text{K}$). To achieve a performance close to the maximum possible at a low NPR, a bell-shaped nozzle should be designed with a low aspect ratio (for example, $\epsilon_e = 10$), but this would imply that for the vast majority of the flight it would work in under-expansion conditions and would provide a very poor performance at low ambient pressure if compared to the isentropic plug nozzle. To achieve a good performance at a high NPR, the bell-shaped nozzle should be designed with a larger aspect ratio (for example, $\epsilon_e = 80$), but this would lead to poor performance at low altitude and, in case the expansion ratio was too large, a normal shock wave could appear inside the engine: Figure 18 reports only the operative range of bell-shaped nozzles; the hatched red region highlights their non-operative conditions. At very low ambient pressure, the ideal plug nozzle also starts to behave like a bell-shaped one with an aspect ratio equal to 100. Therefore, to achieve the highest performance its geometrical aspect ratio should be maximized in order to diverge as late as possible from the behaviour of an optimal expansion nozzle. Hence, the ideal plug nozzle exit section should cover the entire rocket diameter. Due to the results shown in Figure 16, the same design criteria could be applied to the aerospike design.

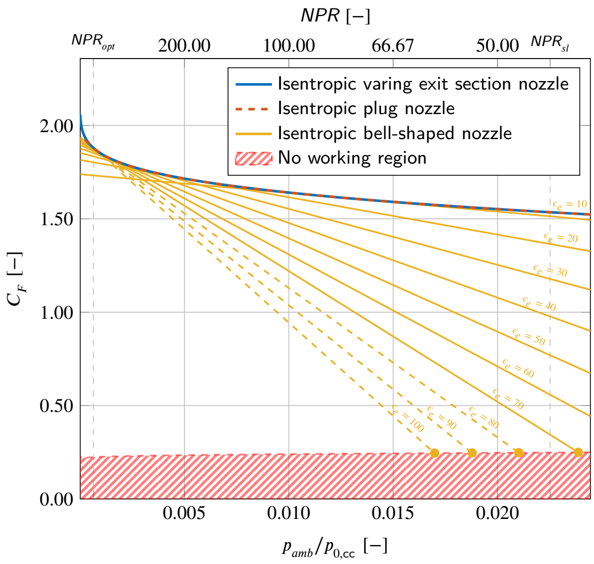

Figure 18. Comparison between different engine performances. The yellow dash lines represent a family of bell-shaped nozzle designed with different aspect ratio.

5.3. Thrust Delivered by Individual Engine Surface

5.3.1. Theoretical Thrust Delivered by Each Surface

To understand the source of the thrust losses highlighted in Figure 16, the thrust delivered by each engine surface has been compared with the corresponding theoretical one. The engine can be divided in eight surfaces, as shown in Figure 19. For each surface, the theoretical thrust coefficient can be evaluated and then compared with the one obtained from the simulation using Equations (30)–(32):

$$\underline{F}_j = \hat{\mathbf{n}}_{ea} \cdot \int_{S_{\text{wall},j}} \left[\left(\underline{p} - p_{amb} \right) \mathrm{I} + \underline{\boldsymbol{\tau}} \right] \hat{\mathbf{n}} \, dA \tag{30}$$

$$\underline{C}_{F,j} = \frac{\underline{F}_j}{A_{th}^{geo} \, p_{0,\text{cc}}} \tag{31}$$

where $\hat{\mathbf{n}}_{ea}$ is the unit vector parallel to the engine axis, pointing toward the engine inlet, $\hat{\mathbf{n}}$ is the outward surface normal unit vector, and $S_{\text{wall},j}$ is the j-th wall surface. The inlet contribution has been evaluated considering a combustion chamber with a finite cross-section area. Therefore, the part of the engine before the inlet has been considered as an ideal nozzle (i.e., inviscid flow and isentropic expansion) whose exit section corresponds to the simulation inlet.

$$\underline{F}_{\text{inlet}} = \hat{\mathbf{n}}_{ea} \cdot \int_{S_{\text{inlet}}} \left[\underline{\rho} \, \underline{\mathbf{u}} (\underline{\mathbf{u}} \cdot \hat{\mathbf{n}}) + \left(\underline{p} - p_{amb} \right) \hat{\mathbf{n}} \right] dA \tag{32}$$

The methodology used to obtain the theoretical thrust coefficients has already been introduced by Fadigati in [33] (Section 5.2.2) for $p_{amb} > p_{amb}^{\mathrm{B}}$. Hence, it will be discussed briefly. Figure 19 shows the engine subdivision in the case in which $p_{amb} > p_{amb}^{\mathrm{B}}$. As shown in [33], applying the momentum balance and the isentropic nozzle theory, the thrust developed by the j-th region can be written as

$$\begin{aligned} F_j = \; & \dot{m} \left(u_{r,j} \cos \theta_{r,j} - u_{l,j} \cos \theta_{l,j} \right) \\ & + \left(p_{r,j} - p_{amb} \right) A_{r,j} \cos \beta_{r,j} \\ & + \left(p_{l,j} - p_{amb} \right) A_{l,j} \cos \beta_{l,j} \end{aligned} \tag{33}$$

where F_j is the thrust delivered by the j-th section, $\dot{m}$ is the mass flow rate, u is the flow speed, θ is the flow inclination with respect to the engine axis (the angle θ is positive when the flow velocity is pointing away from the engine axis), p is the static pressure, A is the engine section area, and β is the angle between the engine section normal and the engine axis (the angle β is positive when $\hat{\mathbf{n}}$ is pointing away from the engine axis). The thrust developed by the part of the engine before the inlet is obtained by applying the isentropic nozzle theory, considering the inlet as a rocket exit section.

$$F_{\text{inlet}} = \dot{m}\, u_{\text{inlet}} + (p_{\text{inlet}} - p_{amb}) A_{\text{inlet}} \tag{34}$$

The mass flow rate $\dot{m}$ can be calculated using the isentropic nozzle theory. It is independent of the ambient pressure because the engine is working in chocked conditions. It is better to split the thrust evaluation into two cases:

- $p_{amb} > p^{\text{B}}_{amb}$: The Prandtl–Meyer expansion ends over the spike;
- $p_{amb} \leq p^{\text{B}}_{amb}$: The Prandtl–Meyer expansion ends at the end of the spike or beyond it.

When $p_{amb} > p^{\text{B}}_{amb}$, the isentropic nozzle theory allows us to estimate the pressure and the velocity in each engine section from the inlet to the line JB′, which marks the end of the expansion, in which the flow reaches the ambient pressure value. After this section, the flow cannot be expanded any more and, therefore, the pressure is considered constant and equal to p_{amb}, while the velocity magnitude is constant and equal to

$$u_{\text{JB}'} = \sqrt{\frac{2\gamma R_s}{\gamma - 1} T_{0,\text{cc}} \left[1 - \left(\frac{p_{amb}}{p_{0,\text{cc}}} \right)^{\frac{\gamma-1}{\gamma}} \right]} \tag{35}$$

The inclinations of the engine section normal unit vector (β) are known a priori, except for $\beta_{\text{JB}'}$, which depends on the ambient pressure. It can be calculated using the Prandtl–Meyer theory (Appendix D).

In this supersonic expansion region, the relation between the area ratio and the local Mach number should be modified as follows:

$$\epsilon = \frac{\mathcal{A}}{A^{geo}_{th}} = \frac{1}{M} \sqrt{\left[\frac{1 + \frac{\gamma-1}{2} M^2}{\frac{\gamma+1}{2}} \right]^{\frac{\gamma+1}{\gamma-1}}} \tag{36}$$

in which $\mathcal{A} = A \sin \xi$: $\mathcal{A}$ is the actual passage area, A is the geometrical area of a generic engine section, and ξ is the local Mach angle, which is also the inclination at which the flow crosses the local Mach line (Appendix D).

From the inlet to the throat section, the flow direction has been assumed to be perpendicular to the corresponding engine section. The flow direction $\theta_{\text{JB}'}$ can be evaluated from the Prandtl–Meyer theory (Appendix D). In agreement with Onofri in [57], in over-expansion conditions, the flow is confined close to the spike. Therefore, when it leaves it, its direction is parallel to the wall itself. This is true until $p_{amb} \approx p^{\text{B}}_{amb}$. In this situation, only the flow close to the spike wall has a direction parallel to the latter. At the same time, the more external flow is oriented according to the Prandtl–Meyer expansion. Therefore, to blend these two conditions, it has been assumed that

$$\theta_{\text{BW}} = \max\left(\delta_{\text{B}}, \theta_{\text{JB}'}\right) \tag{37}$$

By convention, θ is positive when the flow velocity is pointing away from the engine axis. δ is oriented in the same way. Along the line A′V, it has been assumed that the flow is parallel to the engine axis. This condition is the one that maximizes its thrust contribution and allows us to obtain an overall value equal to the one calculated using the isentropic nozzle theory on an equivalent nozzle that has the same aspect ratio, throat section area, and combustion chamber total pressure. The location of point W has been chosen in order to contain all the flow inside the coloured region shown in Figure 19. Hence, there is no mass flow rate through the lines LW and WV.

When $p_{amb} \leq p^{B}_{amb}$, the Prandtl–Meyer expansion covers the entire spike. Therefore, in this condition, the point B′ coincides with B; hence it no longer represents the end of the Prandtl–Meyer expansion, which could continue beyond the spike end. From the inlet surface up to the line JB, the thrust could be evaluated as has been described before because the same hypotheses apply. For the other surfaces, instead, different hypotheses should be adopted. The thrust provided by the spike between the points B′ and B is zero because the surface between these two points collapses into a circle whose lateral surface has zero area. The thrust contribution delivered by the base could be evaluated by applying Equation (33) to the region delimited by the line JBAA′VWL, but this calculation can be skipped because the ideal aerospike can at least work like the ideal plug nozzle, meaning that the base sufficiently contributes to make the aerospike reach the ideal plug nozzle thrust value. Obviously, this is an upper bound for the thrust generated by the base. The estimation of the base thrust coefficient will be deepened in Section 5.3.3.

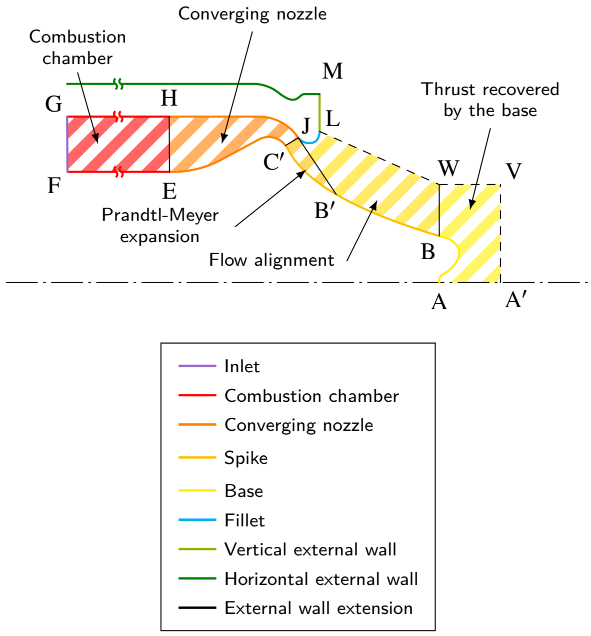

Figure 19. Subdivision of the engine into five regions used to evaluate the thrust produced by each surface when $p_{amb} > p^{B}_{amb}$. (For interpretation of the colours in the figure(s), the reader is referred to the web version of this article.)

According to the Prandtl–Meyer expansion, the point J is a singularity in which the pressure decreases from the throat value to the ambient one. Therefore, the entire fillet feels the ambient pressure and does not contribute to the resulting thrust. Also, the pressure distribution over the vertical and the horizontal external walls is constant and equal to the ambient one. Consequently, they theoretically provide zero thrust at every ambient pressure.

5.3.2. Comparison of the Thrust Coefficients Generated by Each Surface

The comparison between the theoretical results and the ones obtained from the simulations are shown in Figures 20 and 21, which display the thrust coefficient delivered by each engine surface, except for the external wall. The value associated to the latter is, in modulus, lower than 7.6×10^{-4}. Hence, being very close to the null theoretical value, it can be considered negligible in the following analysis. Anyhow, it must be underlined that this thrust coefficient is not exactly zero in the simulation because the aerospike plume sucks the external flow [33,58], leading to wall shear stress formation on the external wall. Figure 20 highlights how, for the inlet, combustion chamber, and converging section, the numerical results remain close to the theoretical predictions, with deviations mainly driven by boundary-layer-induced reductions in mass flow rate. Figure 21 shows instead that the largest discrepancies arise in the spike region and in the fillet. The portion of the spike controlled by the Prandtl–Meyer expansion shows reduced thrust at a low NPR because the expansion is delayed by the rounded fillet. The base contribution matches the theoretical value in under-expanded conditions, while in over-expansion its oscillatory behaviour reflects variations in the flow turning angle after the oblique shock at the spike end (this part will be described more in detail in Section 5.3.3). Figure 22 shows the difference between the thrust coefficients obtained from the simulations and the theoretical ones:

$$\Delta \underline{C}_{F,j} = \underline{C}_{F,j} - C_{F,j} \tag{38}$$

where $C_{F,j}$ and $\underline{C}_{F,j}$ are, respectively, the theoretical thrust coefficient delivered by the j-th surface and the one calculated from the simulation on the same surface. The theoretical thrust developed by the inlet is close to the simulation results because in both cases similar formulas have been used to evaluate it. The difference is mainly due to the mass flow rate reduction due to the boundary layer. The combustion chamber produces a slightly negative thrust coefficient due to the flow boundary layer. At every nozzle pressure ratio, the converging nozzle delivers less drag than the theoretical one. This phenomenon has already been explained by Fadigati in [33], and it will not be investigated here. For $NPR > NPR_{\mathrm{B}}$, the Prandtl–Meyer expansion covers the entire spike. Hence, the pressure distribution over it is independent of the ambient pressure. This explains why the spike thrust coefficient, shown in Figure 21, related to the Prandtl–Meyer expansion grows linearly as the ambient pressure decreases. For $NPR < NPR_{\mathrm{B}}$, the thrust produced by the Prandtl–Meyer expansion starts to decrease because it covers a smaller part of the spike, while the thrust delivered by the alignment of the flow over the spike grows with $\frac{p_{amb}}{p_{0,\mathrm{cc}}}$. The base works close to the theoretical prediction for $NPR > 22.50$, which is almost the transition nozzle pressure ratio that delimits the open-wake condition from the closed-wake one: more details about the transition nozzle pressure ratio are given in Section 5.5. For $NPR < 22.50$, the base produces less thrust than in the theoretical case. In under-expansion conditions, the thrust delivered by the base is positive, and it increases linearly as the ambient pressure decreases. In [57], Onofri claims that the base delivers positive thrust in under-expansion conditions and a neutral or slightly negative contribution in over-expansion. The first part of the sentence is in agreement with the results shown in Figure 21, while in over-expansion conditions the results are in disagreement: this issue is explained in Section 5.3.3. The fillet produces a negative thrust due to the delayed expansion, which has already been described by Fadigati in [33]. Its drag contribution decreases linearly as $\frac{p_{amb}}{p_{0,\mathrm{cc}}}$ increases, reaching almost a null value because, increasing $\frac{p_{amb}}{p_{0,\mathrm{cc}}}$, the area of the fillet covered by the expansion decreases, and the one that feels the ambient pressure increases.

https://doi.org/10.3390/aerospace13010012

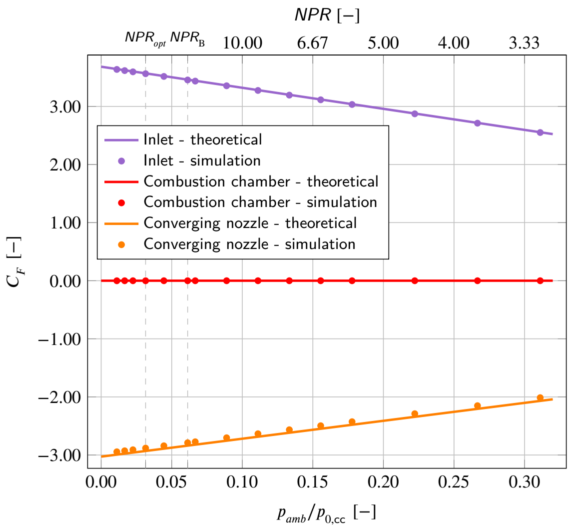

Figure 20. Comparison among the theoretical thrust coefficients of the inlet, the combustion chamber, and the converging nozzle.

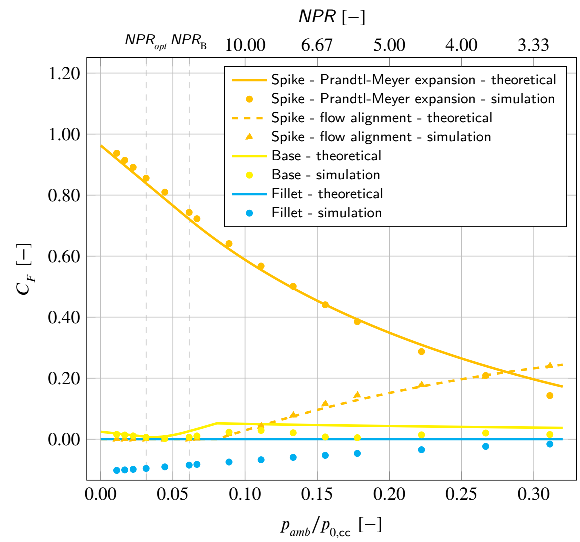

Figure 21. Comparison among the theoretical thrust coefficients of the spike (Prandtl–Meyer expansion), the last portion of it, the base, and the fillet.

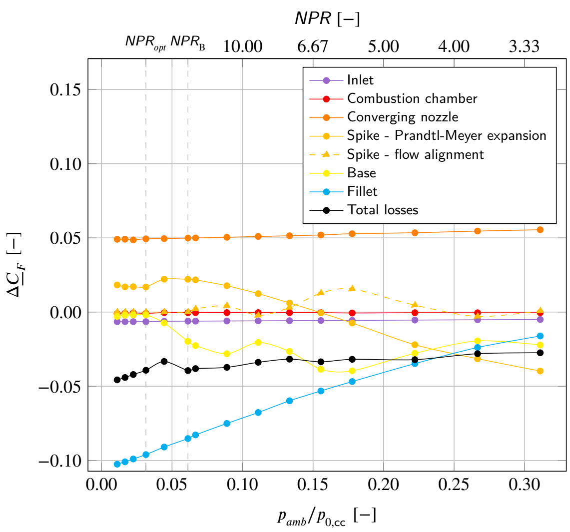

Figure 22. Thrust coefficient difference for each surface varying the *NPR*: $\Delta \underline{C}_{F,j} = \underline{C}_{F,j} - C_{F,j}$.

For $NPR > 4.0$, the fillet provides the highest drag, which is partially compensated by the converging nozzle and the first part of the spike covered by the Prandtl–Meyer expansion. Figure 23 shows the same results divided for the corresponding theoretical thrust coefficient of the engine at a given NPR.

$$\delta \underline{C}_{F,j} = \frac{\Delta \underline{C}_{F,j}}{C_F} = \frac{\underline{C}_{F,j} - C_{F,j}}{C_F} \tag{39}$$

where $C_{F,j}$ and $\underline{C}_{F,j}$ are, respectively, the theoretical thrust coefficient delivered by the j-th surface and the one calculated from the simulation on the same surface. Meanwhile C_F is the total theoretical thrust coefficient:

$$C_F = \sum_j C_{F,j} \tag{40}$$

Under low-ambient-pressure conditions, the fillet decreases the theoretical thrust coefficient by more than 6% relative to its original value. Table 5 collects the $\delta C_{F,j}$ for every surface at the different values of NPR, highlighting the pressure contribution $\delta \underline{C}^{p}_{F,j}$ and the drag due to the wall shear stress $\delta \underline{C}^{wss}_{F,j}$:

$$\underline{C}^{p}_{F,j} = \frac{\underline{F}^{p}_{j}}{A^{geo}_{th}\, p_{0,\mathrm{cc}}} = \frac{\hat{\mathbf{n}}_{ea} \cdot \int_{S_{\mathrm{wall},j}} \left(\underline{p} - p_{amb}\right) \mathrm{I} \cdot \hat{\mathbf{n}}\, dA}{A^{geo}_{th}\, p_{0,\mathrm{cc}}} \tag{41}$$

$$\underline{C}^{wss}_{F,j} = \frac{\underline{F}^{wss}_{j}}{A^{geo}_{th}\, p_{0,\mathrm{cc}}} = \frac{\hat{\mathbf{n}}_{ea} \cdot \int_{S_{\mathrm{wall},j}} \underline{\boldsymbol{\tau}}\hat{\mathbf{n}}\, dA}{A^{geo}_{th}\, p_{0,\mathrm{cc}}} \tag{42}$$

$$\delta \underline{C}^{p}_{F,j} = \frac{\underline{C}^{p}_{F,j} - C_{F,j}}{C_F} \tag{43}$$

$$\delta \underline{C}^{wss}_{F,j} = \frac{\underline{C}^{wss}_{F,j}}{C_F} \tag{44}$$

The theoretical drag related to the wall shear stress is considered zero: $C^{wss}_{F,j} = 0$. The table highlights that the drag due to the wall shear stress is located mainly at the converging nozzle, at the fillet, and on the first part of the spike. The average overall drag contribution among the different NPR values is about -0.75%, while the average thrust loss related to the pressure distribution is about -2.04%, almost three times bigger.

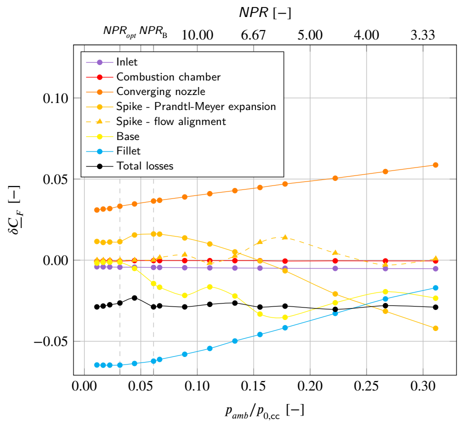

Figure 23. Thrust coefficient difference in percentage with respect the total theoretical thrust coefficient for each surface, varying the NPR: $\delta \underline{C}_{F,j} = \frac{\underline{C}_{F,j} - C_{F,j}}{C_F}$.

Table 5. Summary of the thrust coefficient calculated for every engine surface.

			Inlet		Combustion Chamber		Converging Nozzle		Fillet		Spike Prandtl–Meyer Expansion		Spike Last Part		Base		External Wall		Total			Theoretical
	$p_{amb}/p_{0,cc}$ [−]	NPR [−]	$\delta \underline{C}^{p}_{F,inlet}$ [%]	$\delta \underline{C}^{wss}_{F,inlet}$ [%]	$\delta \underline{C}^{p}_{F,cc}$ [%]	$\delta \underline{C}^{wss}_{F,cc}$ [%]	$\delta \underline{C}^{p}_{F,cn}$ [%]	$\delta \underline{C}^{wss}_{F,cn}$ [%]	$\delta \underline{C}^{p}_{F,fillet}$ [%]	$\delta \underline{C}^{wss}_{F,fillet}$ [%]	$\delta \underline{C}^{p}_{F,spm}$ [%]	$\delta \underline{C}^{wss}_{F,spm}$ [%]	$\delta \underline{C}^{p}_{F,slp}$ [%]	$\delta \underline{C}^{wss}_{F,slp}$ [%]	$\delta \underline{C}^{p}_{F,base}$ [%]	$\delta \underline{C}^{wss}_{F,base}$ [%]	$\delta \underline{C}^{p}_{F,ew}$ [%]	$\delta \underline{C}^{wss}_{F,ew}$ [%]	$\delta \underline{C}^{p}_{F}$ [%]	$\delta \underline{C}^{wss}_{F}$ [%]	δC_F [%]	C_F [−]
Under-exp.	0.01	90.00	−0.41	0.00	0.03	−0.09	3.38	−0.29	−6.35	−0.11	1.52	−0.37	0.00	0.00	−0.17	−0.02	−0.01	0.00	−2.01	−0.87	−2.88	1.59
	0.02	60.00	−0.41	0.00	0.03	−0.08	3.46	−0.31	−6.37	−0.11	1.59	−0.50	0.00	0.00	−0.13	−0.01	0.01	0.00	−1.82	−1.00	−2.83	1.56
	0.02	44.41	−0.42	0.00	0.03	−0.06	3.49	−0.31	−6.36	−0.11	1.64	−0.52	0.00	0.00	−0.12	−0.01	0.01	0.00	−1.73	−1.02	−2.75	1.53
Optimal exp.	0.03	31.76	−0.43	0.00	0.03	−0.09	3.68	−0.36	−6.36	−0.11	1.66	−0.52	0.00	0.00	−0.12	−0.01	−0.01	0.00	−1.55	−1.09	−2.64	1.48
Over-expansion	0.04	22.50	−0.43	0.00	0.03	−0.06	3.75	−0.28	−6.27	−0.10	1.75	−0.20	0.00	0.00	−0.50	−0.01	−0.01	0.00	−1.69	−0.65	−2.33	1.43
	0.06	16.32	−0.45	0.00	0.03	−0.06	3.94	−0.30	−6.13	−0.10	1.82	−0.21	0.01	0.00	−1.44	0.00	0.00	0.00	−2.22	−0.66	−2.88	1.37
	0.07	15.00	−0.45	0.00	0.03	−0.06	3.99	−0.30	−6.03	−0.09	1.81	−0.20	0.16	0.00	−1.66	−0.01	0.00	0.00	−2.16	−0.66	−2.82	1.35
	0.09	11.25	−0.46	0.00	0.03	−0.06	4.21	−0.31	−5.71	−0.09	1.56	−0.19	0.33	0.00	−2.17	−0.01	−0.01	0.00	−2.23	−0.66	−2.88	1.29
	0.11	9.00	−0.47	0.00	0.03	−0.06	4.42	−0.33	−5.36	−0.08	1.17	−0.17	−0.18	−0.01	−1.64	−0.01	−0.04	0.00	−2.07	−0.65	−2.72	1.24
	0.13	7.50	−0.48	0.00	0.03	−0.06	4.62	−0.34	−4.91	−0.08	0.66	−0.15	0.26	−0.01	−2.20	−0.01	0.01	0.00	−2.00	−0.65	−2.65	1.20
	0.16	6.43	−0.49	0.00	0.03	−0.06	4.83	−0.35	−4.51	−0.07	0.10	−0.14	1.11	−0.01	−3.31	−0.02	0.00	0.00	−2.24	−0.65	−2.89	1.16
	0.18	5.62	−0.50	0.00	0.03	−0.09	5.06	−0.36	−4.10	−0.07	−0.53	−0.13	1.42	−0.04	−3.51	−0.01	−0.01	0.00	−2.14	−0.69	−2.83	1.12
	0.22	4.50	−0.51	0.00	0.03	−0.07	5.44	−0.38	−3.22	−0.06	−1.98	−0.10	0.50	−0.06	−2.62	−0.01	0.02	0.00	−2.35	−0.68	−3.03	1.06
	0.27	3.75	−0.52	0.00	0.03	−0.08	5.87	−0.41	−2.33	−0.05	−3.08	−0.07	−0.26	−0.04	−1.94	−0.01	0.08	0.00	−2.15	−0.66	−2.81	1.00
	0.31	3.21	−0.53	0.00	0.03	−0.08	6.30	−0.43	−1.66	−0.04	−4.15	−0.05	0.14	−0.05	−2.33	−0.01	−0.03	0.00	−2.24	−0.67	−2.90	0.95

5.3.3. Theoretical Thrust Coefficient Delivered by the Base

To understand the behavior of $C_{F,\text{base}}$ at different nozzle pressure ratios, it is necessary to calculate it using the momentum theory. When $\frac{p_{amb}^{\text{B}}}{p_{0,\text{cc}}} < \frac{p_{amb}}{p_{0,\text{cc}}} \leq \frac{p_{amb}^{cr}}{p_{0,\text{cc}}}$, where $\frac{p_{amb}^{cr}}{p_{0,\text{cc}}}$ is the maximum pressure ratio for which the flow still reaches the sonic condition at the throat section, Equation (33) can be applied to the region BAA′VW considering that the flow enters from the segment BW and exits from A′V: point W has been chosen to fall outside the supersonic flow. In this condition, the expansion has already reached the ambient pressure over the spike, and the base can only recover the thrust due to flow alignment. This implies that the flow speed is constant and equal to $u_{\text{JB}'}$, which is the flow speed at the end of the Prandlt–Meyer expansion (Equation (35)). The flow along the segment BW, according to Equation (37), has an inclination that is the maximum between the spike slope and the flow direction at the end of the Prandtl–Meyer expansion.

When $\frac{p_{amb}}{p_{0,\text{cc}}} \leq \frac{p_{amb}^{\text{B}}}{p_{0,\text{cc}}}$, Equation (33) has to be applied to the region defined by the vertices JBAA′VWL, supposing that the fillet surface feels only the ambient pressure; i.e., it provides zero thrust. Hence, the flow enters from the segment JB and exits from the line LWVA′. In this case, the Prandtl–Meyer expansion has reached the spike end; therefore $u_{\text{JB}'} = u_{\text{JB}}$, and it is independent of $\frac{p_{amb}}{p_{0,\text{cc}}}$.

$$u_{\text{JB}} = \sqrt{\frac{2\gamma R_s}{\gamma - 1} T_{0,\text{cc}} \left[1 - \left(\frac{p_{amb}^{\text{B}}}{p_{0,\text{cc}}} \right)^{\frac{\gamma-1}{\gamma}} \right]} \tag{45}$$

The flow direction along the segment JB is obtained with Equation (37). The pressure over it is fixed at the value p_{amb}^{B}, while, over the exit surface, the flow is expanded down to the maximum between p_{amb}^{opt} and the current ambient value. This happens because the aerospike, like the plug nozzle, looses its adaptability for ambient pressures lower than p_{amb}^{opt}. Hence, the minimum pressure achievable at the end of the expansion is limited by p_{amb}^{opt}: the flow will continue to expand in the atmosphere, but this expansion will have no influence on the thrust delivered by the engine. The flow speed at the exit surface is evaluated as follows:

$$u_e = \sqrt{\frac{2\gamma R_s}{\gamma - 1} T_{0,\text{cc}} \left\{ 1 - \left[\frac{\max\left(p_{amb}, p_{amb}^{opt}\right)}{p_{0,\text{cc}}} \right]^{\frac{\gamma-1}{\gamma}} \right\}} \tag{46}$$

At every nozzle pressure ratio, it has been supposed that the flow exiting from the surface LWVA′ is always aligned with the engine axis because this condition maximizes the thrust; i.e., $C_{F,\text{base}}$ is an upper bound value for the base thrust coefficient. Combining the hypotheses listed before, the base thrust coefficient could be evaluated at different nozzle pressure ratios, as shown in Equation (47).

$$C_{F,\text{base}} = \begin{cases} \frac{\dot{m}}{A_{th}^{geo} p_{0,\text{cc}}} \left[u_{\text{JB}'} - u_{\text{JB}'} \cos\left(\max\left(\delta_{\text{B}}, \theta_{\text{JB}'}\right)\right)\right] & \frac{p_{amb}^{\text{B}}}{p_{0,\text{cc}}} < \frac{p_{amb}}{p_{0,\text{cc}}} \leq \frac{p_{amb}^{cr}}{p_{0,\text{cc}}} \\ \frac{\dot{m}}{A_{th}^{geo} p_{0,\text{cc}}} \left[u_e - u_{\text{JB}} \cos\left(\max\left(\delta_{\text{B}}, \theta_{\text{JB}}\right)\right)\right] - \left(\frac{p_{amb}^{\text{B}}}{p_{0,\text{cc}}} - \frac{p_{amb}}{p_{0,\text{cc}}} \right)\left(\epsilon_e - \frac{A_{\text{base}}}{A_{th}^{geo}} \right) & \frac{p_{amb}^{opt}}{p_{0,\text{cc}}} \leq \frac{p_{amb}}{p_{0,\text{cc}}} \leq \frac{p_{amb}^{\text{B}}}{p_{0,\text{cc}}} \\ \frac{\dot{m}}{A_{th}^{geo} p_{0,\text{cc}}} \left[u_e - u_{\text{JB}} \cos\left(\max\left(\delta_{\text{B}}, \theta_{\text{JB}}\right)\right)\right] - \left(\frac{p_{amb}^{\text{B}}}{p_{0,\text{cc}}} - \frac{p_{amb}}{p_{0,\text{cc}}} \right)\left(\epsilon_e - \frac{A_{\text{base}}}{A_{th}^{geo}} \right) + \left(\frac{p_{amb}^{opt}}{p_{0,\text{cc}}} - \frac{p_{amb}}{p_{0,\text{cc}}} \right)\epsilon_e & \frac{p_{amb}}{p_{0,\text{cc}}} < \frac{p_{amb}^{opt}}{p_{0,\text{cc}}} \end{cases} \tag{47}$$

Here, $A_{\text{base}} = \pi r_{\text{B}}^2$, $A_e = \pi r_{\text{J}}^2$, δ_{B} is the spike slope at point B, while θ_{JB} is the flow direction along the segment JB due to the Prandtl–Meyer expansion. The ratio $\frac{\dot{m}}{A_{th}^{geo}\, p_{0,\text{cc}}}$ can be expanded into

$$\frac{\dot{m}}{A_{th}^{geo}\, p_{0,\text{cc}}} = \frac{\sqrt{\gamma}}{\sqrt{R_s T_{0,\text{cc}}}} \left(\frac{2}{\gamma+1}\right)^{\frac{\gamma+1}{2(\gamma-1)}} \tag{48}$$

Therefore, in Equation (47), p_{amb} always appears divided by $p_{0,\text{cc}}$. Consequently, their ratio can be considered as a unique input parameter for the equation.

$$C_{F,\text{base}} = C_{F,\text{base}}\left(\epsilon_{\text{B}}, \epsilon_e, \frac{p_{amb}}{p_{0,\text{cc}}}, T_{0,\text{cc}}, \gamma, R_s\right) \tag{49}$$

Figure 24 shows the theoretical thrust coefficient of the DemoP1 base, highlighting the contribution of the term related to the pressure and the one related to the velocity variation. For $NPR > NPR_{\delta_{\text{B}}=\theta_{\text{JB}'}}$, the base recovers thrust, aligning the flow with the engine axis. Since the flow leaves the spike with higher speed, its thrust coefficient grows as the ambient pressure decreases, while the pressure term is zero because the flow has already reached the ambient pressure value over the spike. At $NPR_{\delta_{\text{B}}=\theta_{\text{JB}'}} = 12.43$, $\delta_{\text{B}} = \theta_{\text{JB}'}$; hence the flow inclination given by the spike slope is the same as the one given by the Prandtl–Meyer expansion. At this nozzle pressure ratio, there is a discontinuity in the derivative of $C_{F,\text{base}}$ with respect to $\frac{p_{amb}}{p_{0,\text{cc}}}$ due to the presence of the term $\max\left(\delta_{\text{B}}, \theta_{\text{JB}'}\right)$ in Equation (47). Subsequently, for greater nozzle pressure ratios, the thrust coefficient of the base drops because the flow leaves the spike with lower inclination, causing less thrust to be recovered. For $NPR_{\text{B}} < NPR < NPR_{opt}$, the term related to the velocity starts to rise due to the fact that the spike has reached the maximum expansion and the base begins to further expand the flow. Nonetheless, since the pressure term also starts to decrease linearly as $\frac{p_{amb}}{p_{0,\text{cc}}}$ decreases, this is not enough to increase the overall thrust coefficient value. For $NPR > NPR_{opt}$, because the base cannot further expand the flow, the term related to the velocity becomes constant, while the pressure term starts to increase, leading to a rise in the base thrust coefficient with a constant slope equal to $-\frac{A_{\text{base}}}{A_{th}^{geo}}$:

$$-\frac{A_{\text{base}}}{A_{th}^{geo}} = -\frac{A_{\text{base}}}{A_e}\frac{A_e}{A_{th}^{geo}} = -\frac{\pi r_{\text{B}}^2}{\pi r_e^2}\epsilon_e = -\eta_b^2 \epsilon_e \tag{50}$$

where $\eta_b = \frac{r_{\text{B}}}{r_e}$. From Figure 24, it is clear that the theory matches the simulation results in under-expansion conditions, while it overpredicts the thrust coefficient in the other cases. The main issue is the estimation of the flow direction at the spike end. In over-expansion conditions, the flow after the Prandtl–Meyer expansion deviates due to a series of oblique shock waves and expansion fans: in particular in DemoP1 there is only one oblique shock wave because the spike is relatively short. After this shock wave, most of the flow keeps the new direction independently of the spike wall. As can be seen from Figure 12, most of the flow leaves the spike with an inclination larger than δ_{B}, i.e., more aligned to the engine axis. In over-expansion conditions, $\underline{C}_{F,\text{base}}$ oscillates due to the oblique shock over the spike, which influences the flow direction. An opposite oscillation can be seen in Figure 21 in the thrust coefficient of the last part of the spike. To confirm this hypothesis, an average value of the flow inclination over the segment BW can be computed using the following formulas:

$$\underline{\tilde{\mathbf{u}}}_{\mathrm{BW}}(t) = \frac{\int_{S_{\mathrm{BW}}} \underline{\rho}(\mathbf{x},t)\,\underline{\mathbf{u}}(\mathbf{x},t)(\underline{\mathbf{u}}(\mathbf{x},t)\cdot\hat{\mathbf{n}})\,dS}{\int_{S_{\mathrm{BW}}} \underline{\rho}(\mathbf{x},t)\,(\underline{\mathbf{u}}(\mathbf{x},t)\cdot\hat{\mathbf{n}})\,dS} = \frac{\int_{S_{\mathrm{BW}}} \underline{\rho}(\mathbf{x},t)\,\underline{\mathbf{u}}(\mathbf{x},t)(\underline{\mathbf{u}}(\mathbf{x},t)\cdot\hat{\mathbf{n}})\,dS}{\underline{\dot{m}}(t)} \tag{51}$$

$$\underline{\tilde{\theta}}_{\mathrm{BW}}(t) = \mathrm{atan2}(\hat{\mathbf{r}}\cdot\underline{\tilde{\mathbf{u}}}_{\mathrm{BW}}(t), \hat{\imath}\cdot\underline{\tilde{\mathbf{u}}}_{\mathrm{BW}}(t)) \tag{52}$$

$$\underline{\hat{\theta}}_{\mathrm{BW}} = \frac{1}{\Delta t_{\mathrm{pp}}}\int_{t_a}^{t_b} \underline{\tilde{\theta}}_{\mathrm{BW}}(t)\,dt \tag{53}$$

where $\hat{\imath}$ and $\hat{\mathbf{r}}$ are the unit vectors pointing, respectively, along the engine axis and along the radial direction. t_a and t_b are the extreme values of the post-processing time interval: $\Delta t_{pp} = t_b - t_a$. They are, respectively, equal to 60 ms and 70 ms. The average computed with Equation (52) has been designed in order to conserve the instantaneous momentum flux through the surface S_{BW}:

$$\underline{\tilde{\boldsymbol{\mathcal{F}}}}_{\mathrm{BW}}(t) = \int_{S_{\mathrm{BW}}} \underline{\rho}(\mathbf{x},t)\,\underline{\mathbf{u}}(\mathbf{x},t)(\underline{\mathbf{u}}(\mathbf{x},t)\cdot\hat{\mathbf{n}})\,dS \tag{54}$$

As shown by Figure 24, for $NPR < NPR_{\mathrm{B}}$, $\underline{\hat{\theta}}_{\mathrm{BW}}$ oscillates in the opposite direction to $\underline{C}_{F,\mathrm{base}}$, confirming their negative correlation. When $\underline{\hat{\theta}}_{\mathrm{BW}}$ has a low value, the flow leaves the spike with an inclination towards the engine axis. Therefore, $\underline{C}_{F,\mathrm{base}}$ is high because the flow has to turn by a greater angle to align it with the axial direction. In the opposite case, when $\underline{\hat{\theta}}_{\mathrm{BW}}$ is almost horizontal, less thrust can be recovered by the base. Figure 24 also highlights how the hypothesis that, in over-expansion conditions, the flow leaves the spike parallel to its wall is not completely true. Only the flow portion close to the wall is influenced by the wall slope, while, far away from it, its direction depends on the deviation due to the last shock/expansion waves over the spike. $\underline{\hat{\theta}}_{\mathrm{BW}}$ oscillates with varying ambient pressures because a supersonic flow cannot follow the smooth wall variation,but it can only turn by means of shock waves. Despite that, the approximation

$$\theta_{\mathrm{BW}} = \max\left(\delta_{\mathrm{B}}, \theta_{\mathrm{JB}'}\right) \tag{55}$$

used in Equation (47), for $\frac{p^{\mathrm{B}}_{amb}}{p_{0,\mathrm{cc}}} < \frac{p_{amb}}{p_{0,\mathrm{cc}}} \leq \frac{p^{cr}_{amb}}{p_{0,\mathrm{cc}}}$, is accurate enough to obtain an upper bound for the base thrust coefficient.

The DemoP1 base thrust coefficient reaches higher values in the over-expansion conditions than the under-expansion ones. This is in disagreement with Onofri, who, in [57], claims that the base delivers positive thrust in under-expansion conditions and a neutral or slightly negative contribution in over-expansion. This discrepancy is due to two aspects. The first one is the low aspect ratio of DemoP1, which reduces the slope of the thrust coefficient with respect $\frac{p_{amb}}{p_{0,\mathrm{cc}}}$ in under-expansion conditions. The second aspect is related to the limits of the theory shown in this section. It is not able to predict the losses related to the flow detachment at the spike end. Therefore, it will never predict a negative thrust.

https://doi.org/10.3390/aerospace13010012

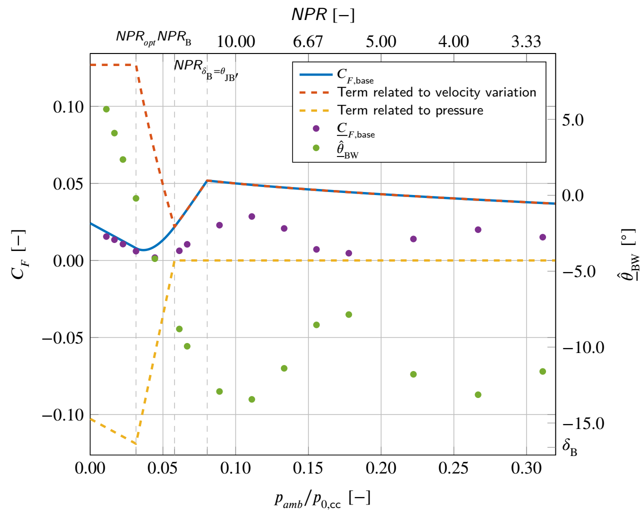

Figure 24. Base thrust coefficient components and flow velocity inclination along the segment BW. The lines represent the theoretical data, while the dots correspond to their respective simulations.

5.4. Spike

Pressure Distribution

Figure 25 shows the pressure distribution over the spike at different nozzle pressure ratios, highlighting with a triangular mark the theoretical point at which the Prandtl–Meyer expansion ends. In Figure 25, the coloured band represents the range of one standard deviation above and below the mean pressure (the standard deviation is very small; hence only for certain NPR values is it visible in Figure 25). It has been evaluated between 60 ms and 70 ms. s_{th} and s_B are, respectively, the curvilinear coordinate of the throat section and the one of the base, which starts from point B. The light grey dash-dotted line represents the theoretical isentropic pressure distribution up to the corresponding ambient pressure. Close to s_{th}, the pressure decreases and then increases due to the phenomenon related to the shape of the sonic line in the throat section, as explained by Fadigati in [33]. This phenomenon, which leads to a lower pressure at the beginning of the spike, explains why, for low nozzle pressure ratios, the portion of wall covered by the Prandtl–Meyer expansion delivers less thrust than the theoretical one. In agreement with the results shown by Fadigati in [33], in every simulation, after the pressure peak near the throat section, the pressure distribution over the spike is higher than the theoretical one due to the expansion delay introduced by the fillet JL [33], shown in Figure 3. Figure 26 shows the relative pressure distribution over the spike, defined as $p - p_{amb}$—this representation better highlights that the expansion fan always ends at a pressure slightly higher than ambient: also in this case the triangular marks indicate the theoretical end of the Prandtl–Meyer expansion. After the Prandtl–Meyer expansion, the pressure increases again due to a small flow detachment already explained by Fadigati in [33]. The flow separation is followed by an oblique shock, visible in Figures 4 and 5, which deviates the flow, increasing its pressure. After the compression wave the pressure slightly rises linearly with the coordinate s. For the simulations with $NPR \leq 6.43$, the oblique shock reflection reaches the spike wall, while, in the other cases, it spreads beyond the spike. This effect is visible in Figure 26 because the pressure quickly drops before the end of the spike (s_B).

Decreasing the ambient pressure, the Prandtl–Meyer expansion end moves towards the final portion of the spike. For $NPR = 16.32$, it reaches point B. For higher nozzle pressure ratios, the pressure distribution over the spike is constant. Therefore, the optimal expansion condition cannot be achieved over the spike itself.

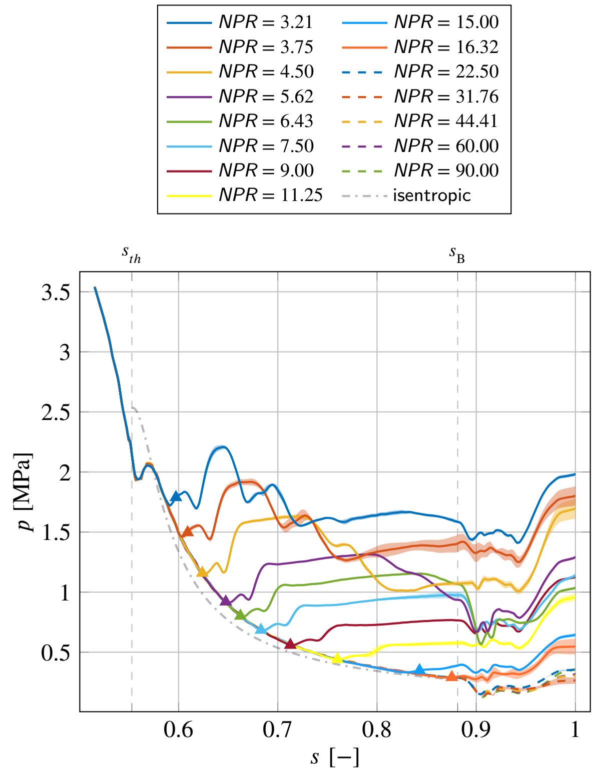

Figure 25. Pressure distribution over the spike and the base compared with the isentropic results obtained by combining Angelino's theory and the isentropic nozzle theory. The triangular marks highlight the theoretical point at which the Prandtl–Meyer expansion ends.

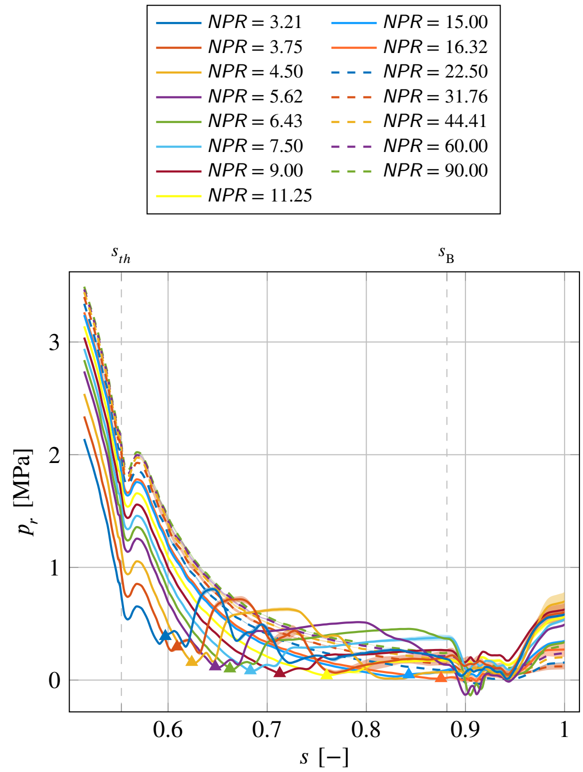

Figure 26. Relative pressure distribution over the spike and the base compared with the isentropic results obtained by combining Angelino's theory and the isentropic nozzle theory. The triangular marks highlight the theoretical point at which the Prandtl–Meyer expansion ends.

5.5. Base

5.5.1. Pressure Distribution

Figure 27 shows the pressure distribution along the base normalized by its ambient value. In each simulation, after the spike end, the pressure drops and remains almost constant down to $r = 10\,\mathrm{mm}$. Below this threshold, it increases, reaching a value higher than ambient near the engine axis. For NPR higher than 31.76, the aerospike loses its adaptability feature. Therefore, the pressure at the base cannot reach the ambient value anymore, becoming much higher. The pressure distribution shown in Figure 27 has a similar trend to that reported by Chutkey in [59] (Figure 13).

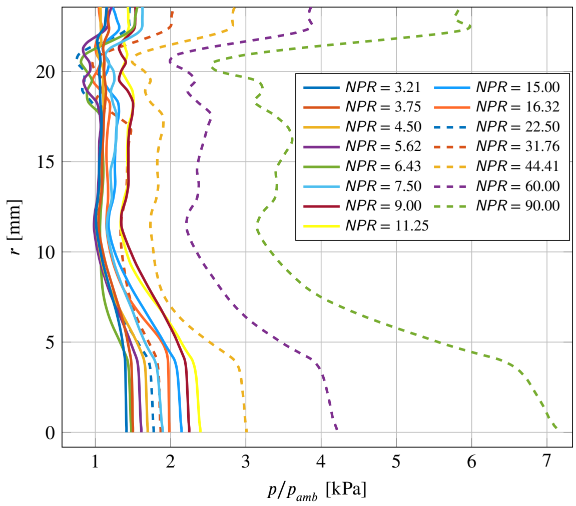

Figure 27. Radial distribution of the ratio between the pressure at the aerospike base and the ambient pressure.

5.5.2. Recirculating Bubble

Figures 12–15 highlight the presence of a recirculation bubble in front of the aerospike base. Its length can be estimated using the studies performed by Chang and Herrin in [60,61] on the axisymmetric supersonic backward-facing step. They concluded that for a flow with a Mach number higher than 2, the length of the recirculating bubble is $l_{rb} \approx 2.65 r_{\mathrm{B}}$, where r_{B} is the radial coordinate of the point B. Using the isentropic nozzle theory, this condition is met for $NPR > 7.54$. In [56], Onofri corrected this formula with the wall slope at point B:

$$l_{rb} = \left(2.65 - 0.00144\delta_{\mathrm{B}}^2\right) r_{\mathrm{B}} \tag{56}$$

where δ_{B} is the wall slope at the spike end. Figure 28 compares the average length of the recirculation bubble obtained from the simulation with the one predicted using the two previous models: the error bars represent the minimum and maximum bubble lengths during the post-processing time interval. $\underline{l}_{rb}$ is calculated as the length of the segment AA$''$. In under-expansion conditions, the two models are close to the recirculating bubble length obtained from the simulations, but they cannot explain the decreasing trend for increasing NPR. The length of the recirculating bubble is driven by two phenomena. As shown in Figure 26, at each nozzle pressure ratio, the pressure at point B is equal to or slightly higher than ambient. Therefore, the flow at the spike end further expands, turning towards the base. After this expansion, its direction could be evaluated as follows:

- $\frac{p^{\mathrm{B}}_{amb}}{p_{0,\mathrm{cc}}} < \frac{p_{amb}}{p_{0,\mathrm{cc}}}$: the flow is confined close to the spike wall. Hence, an average pressure value along the segment BW could be evaluated as

$$\tilde{\underline{p}}_{\mathrm{BW}}(t) = \frac{\int_{S_{\mathrm{BW}}} \underline{p}(\mathbf{x},t)\underline{\rho}(\mathbf{x},t)(\underline{\mathbf{u}}(\mathbf{x},t)\cdot\hat{\mathbf{n}})\,dS}{\int_{S_{\mathrm{BW}}} \underline{\rho}(\mathbf{x},t)(\underline{\mathbf{u}}(\mathbf{x},t)\cdot\hat{\mathbf{n}})\,dS} = \frac{\int_{S_{\mathrm{BW}}} \underline{p}(\mathbf{x},t)\underline{\rho}(\mathbf{x},t)(\underline{\mathbf{u}}(\mathbf{x},t)\cdot\hat{\mathbf{n}})\,dS}{\underline{\dot{m}}(t)} \tag{57}$$

where $\underline{\dot{m}}(t)$ is the instantaneous mass flow rate. Point W always lies above the shear layer. $\tilde{\underline{p}}_{\mathrm{BW}}$ is used to evaluate an average Mach number

$$\tilde{\underline{M}}_{\mathrm{BW}}(t) = \sqrt{\frac{2}{\gamma-1}\left[\left(\frac{p_{0,\mathrm{cc}}}{\tilde{\underline{p}}_{\mathrm{BW}}(t)}\right)^{\frac{\gamma-1}{\gamma}} - 1\right]} \tag{58}$$

The new average flow direction could be evaluated by applying the Prandlt–Meyer expansion theory and then averaging over the time,

$$\hat{\underline{\theta}}_{\mathrm{B}*} = \frac{1}{\Delta t_{\mathrm{pp}}}\int_{t_a}^{t_b}\left\{\tilde{\underline{\theta}}_{\mathrm{BW}}(t) - \left[\nu(M_e) - \nu\left(\tilde{\underline{M}}_{\mathrm{BW}}(t)\right)\right]\right\}dt \tag{59}$$

where $\underline{\theta}_{\mathrm{B}*}$ is the flow direction after the expansion while $\tilde{\underline{\theta}}_{\mathrm{BW}}$ is calculated using Equations (51) and (52).

- $\frac{p^{\mathrm{B}}_{amb}}{p_{0,\mathrm{cc}}} \geq \frac{p_{amb}}{p_{0,\mathrm{cc}}}$: only the flow close to the aerospike has an influence on the bubble length. Therefore, the procedure is similar to the one presented before, but $\tilde{\underline{p}}_{\mathrm{BW}}$ and $\tilde{\underline{\theta}}_{\mathrm{BW}}$ are substituted with the pressure at point B and δ_{B}, where the latter is the slope of the spike at point B itself.

$$\underline{M}_{\mathrm{B}}(t) = \sqrt{\frac{2}{\gamma-1}\left[\left(\frac{p_{0,\mathrm{cc}}}{\underline{p}_{\mathrm{B}}(t)}\right)^{\frac{\gamma-1}{\gamma}} - 1\right]} \tag{60}$$

$$\hat{\underline{\theta}}_{\mathrm{B}*} = \frac{1}{\Delta t_{\mathrm{pp}}}\int_{t_a}^{t_b}\{\delta_{\mathrm{B}} - [\nu(M_e) - \nu(\underline{M}_{\mathrm{B}}(t))]\}\,dt \tag{61}$$

In both cases, M_e is the Mach number at the exit section, and according to Equation (46)

$$M_e = \sqrt{\frac{2}{\gamma-1}\left[\left(\frac{p_{0,\mathrm{cc}}}{\max\left(p_{amb}, p^{opt}_{amb}\right)}\right)^{\frac{\gamma-1}{\gamma}} - 1\right]} \tag{62}$$

Figure 28 shows also the estimated $\hat{\underline{\theta}}_{\mathrm{B}*}$, which changes in agreement with the recirculation bubble length: when it has a low value, the recirculating bubble is short, while, in the opposite case, it is elongated. Hence, there is a correlation between these two parameters.

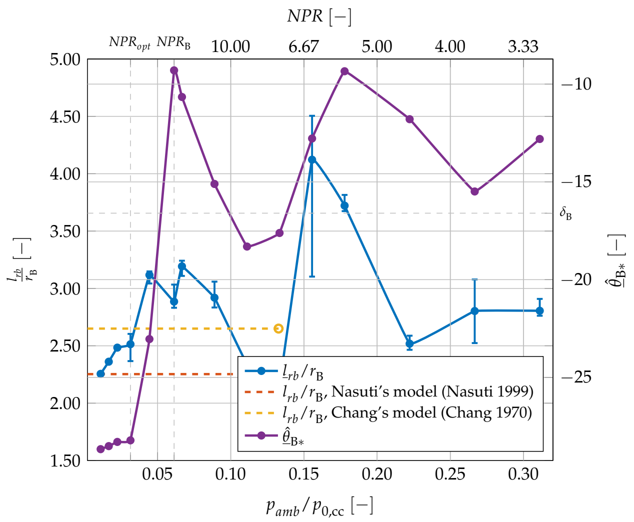

Figure 28. Dimensionless average recirculating bubble length compared with the models shown in [56,60]. The error bars represent the minimum and maximum bubble lengths. The violet line represents the estimated flow direction after the expansion beyond the spike end.

The recirculating bubble length is also driven by the shock wave generated by the reflection of the expansion after point B. When it reaches the inner shear layer like in Figure 29, a Shock Wave–Boundary Layer Interaction (SWBLI) occurs. The adverse pressure gradient induced by the shock wave increases the recirculation bubble length. In the opposite case, shown in Figure 30, the shock wave reaches the engine axis far away from the reattachment region of the flow, and the recirculating bubble length is not affected by it.

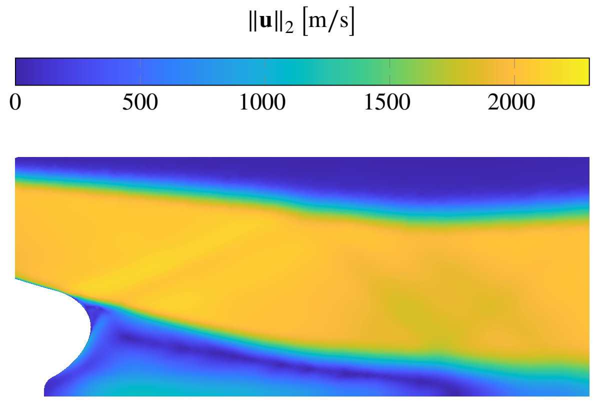

Figure 29. Velocity magnitude field, extracted at $t = 65\,\text{ms}$, of the DemoP1 simulation with $NPR = 5.62$, $p_{amb}/p_{0,cc} = 0.178$.

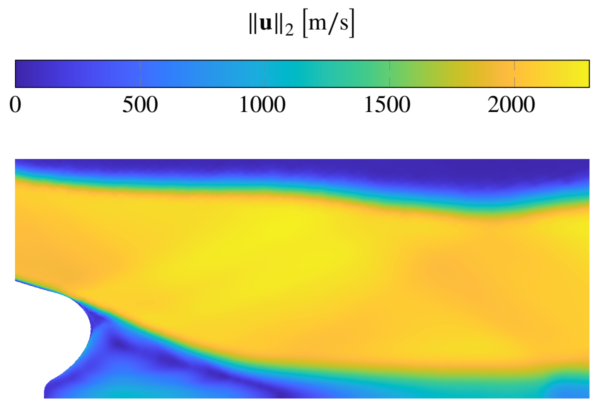

Figure 30. Velocity magnitude field, extracted at $t = 65\,\text{ms}$, of the DemoP1 simulation with $NPR = 7.50$, $p_{amb}/p_{0,cc} = 0.133$.

5.5.3. Open- and Closed-Wake Conditions

According to the definition given by Onofri in [57], the presence of an open-wake structure corresponds to a base pressure dependency on the ambient one, while, in the case of the closed-wake regime, such dependency does not manifest. Looking at Figure 25, it is clear that the transition between these two wake structures happens for an *NPR* value included between 16.32 (NPR_{B}) and 22.50. According to Nasuti and Onofri [56,57], the wake transition occurs when the last characteristic line generated by the Prandtl–Meyer expansion reaches the reattachment point (A$''$), located after the recirculating bubble in front of the aerospike base. Using the equations shown by Nasuti and Onofri in [56,57], it is possible to evaluate the slope of this last characteristic line and evaluate the transition nozzle pressure ratio: $NPR_{tr} = 17.14$, which falls in the previously estimated range. The average length of the recirculating bubble, used in the previous calculation, has been computed among the simulations with $NPR \geq NPR_{\mathrm{B}}$. Figure 31 shows the average pressure at the base obtained using the following equation:

$$\hat{\underline{p}}_{\mathrm{base}} = \frac{\int_{S_{\mathrm{base}}} \underline{p}_{\mathrm{base}}\, dS}{\int_{S_{\mathrm{base}}} dS} \tag{63}$$

From this plot, since the average base pressure is almost constant and independent of the ambient one, it is clear that the aerospike is working in the *closed-wake* condition for $NPR \geq 22.50$. Instead, for nozzle pressure ratios lower than 22.50, the average base pressure rises with the ambient one. Therefore, the engine is working in an *open-wake* condition. In addition, this plot confirms that the actual transition happens in the nozzle pressure ratio range that goes from 16.32 up to 22.50. Differently from the results shown by Onofri in [57], the average base pressure does not grow monotonically as the ambient pressure increases, but for $9.00 \leq NPR \leq 22.50$ it grows faster. This phenomenon is related to the base thrust coefficient oscillation described in Section 5.3.3.

In closed-wake conditions, the base pressure can be estimated using two empirical relations (Equations (64) and (65)) introduced by Fick in [62]. They have been obtained in a cold-flow scenario, but the respective results are very close to those of the simulations performed in this context.

$$\hat{p}_{\mathrm{base}} = p_{\mathrm{B}} \left[0.025 + \frac{0.906}{1 + \frac{\gamma - 1}{2} M_{\mathrm{B}}^2} \right]^{0.35} = 0.22\,\mathrm{MPa} \tag{64}$$

$$\begin{aligned} \hat{p}_{\mathrm{base}} &= p_{\mathrm{B}} M_{\mathrm{B}} \left(\frac{2}{\gamma + 1} \right)^{\frac{\gamma}{\gamma - 1}} \left[0.05 + \frac{0.967}{1 + \frac{\gamma - 1}{2} M_{\mathrm{B}}^2} \right] \\ &= 0.24\,\mathrm{MPa} \end{aligned} \tag{65}$$

where p_{B} and M_{B} are, respectively, the pressure and the Mach number evaluated at the spike end using the isentropic nozzle theory.

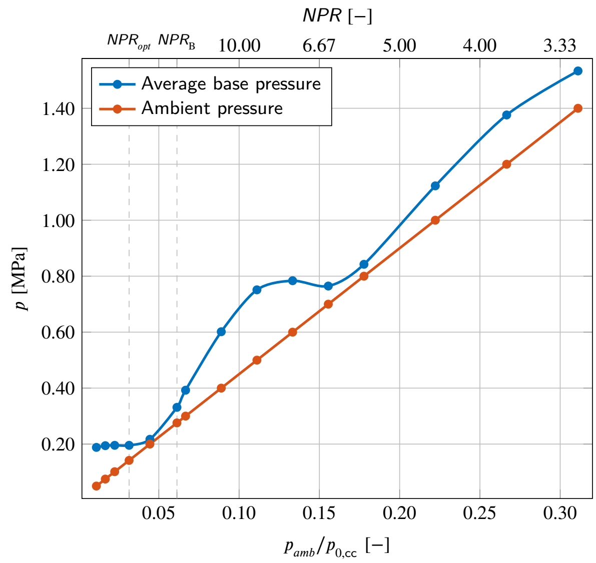

Figure 31. Average pressure distribution at the aerospike base for different nozzle pressure ratios.

6. Flow Separation at the Fillet

After the throat section, the flow expands according to the Prandtl–Meyer expansion. The overall turning angle from throat section is

$$\Delta\theta_{amb} = \theta_{amb} - \theta_{th} = \nu(M_{amb}) \tag{66}$$

where θ_{amb} and θ_{th} are, respectively, the flow inclination with respect to the engine axis at the end of the Prandtl–Meyer expansion and at the throat section. M_{amb} is the Mach number at the end of the Prandtl–Meyer expansion, and it can be evaluated using Equation (67).

$$M_{amb} = \sqrt{\frac{2}{\gamma - 1}\left[\left(\frac{p_{0,\mathrm{cc}}}{p_{amb}}\right)^{\frac{\gamma-1}{\gamma}} - 1\right]} \tag{67}$$

M_{amb} is used instead of M_e because, in the most general case, the flow continues to expand until it reaches the ambient pressure independently on p_{amb}^{opt}. Apparently, for $p_{amb} < p_{amb}^{opt}$, the expansion will continue beyond the spike end. The dependency of $\Delta\theta_{amb}$ on the ambient pressure implies that the flow separates from the fillet at different points depending on the ambient conditions. The location of the separation point can be calculated by finding the curvilinear coordinate, along the fillet wall, for which the projection of the wall shear stress along the wall tangent direction becomes zero.

$$\hat{\tau}_w(s) = \hat{\mathbf{n}}_w^T(s)\underline{\hat{\boldsymbol{\tau}}}_w(s) \cdot \hat{\mathbf{t}}_w(s) \tag{68}$$

where s is a curvilinear coordinate following the fillet wall starting from point J ($s_{th} = s_{\mathrm{J}} = 0$) up to point L ($s_{\mathrm{L}} = 1$), $\hat{\tau}_w$ is defined as the projection of the wall shear stress along the wall tangent direction, $\hat{\mathbf{n}}_w$, $\hat{\mathbf{t}}_w$ are, respectively, the unit vector normal and tangent to the fillet, and $\underline{\hat{\boldsymbol{\tau}}}_w$ is the shear stress tensor evaluated at the wall and averaged in the time intervals t_a and t_b: $t_a = 60\,\mathrm{ms}$ and $t_b = 70\,\mathrm{ms}$. Figure 32 shows the wall shear stress along the fillet wall, highlighting the separation point with a square mark. The upper picture displays a magnification of the fillet, pointing out the location of the separation point. Increasing NPR, the expansion fan turns the flow more, making it follow the fillet wall more; hence the flow separation is delayed along the wall, as is shown in the small picture in Figure 32. $\hat{\tau}_w$ has a similar distribution at every NPR. It rises almost linearly after s_{th} because the bulk velocity of the flow increases due to the expansion. After its maximum value it starts to decrease linearly, and then it drops quickly before the flow separation point. After this, it becomes almost zero because outside the engine plume the gas is almost stationary.

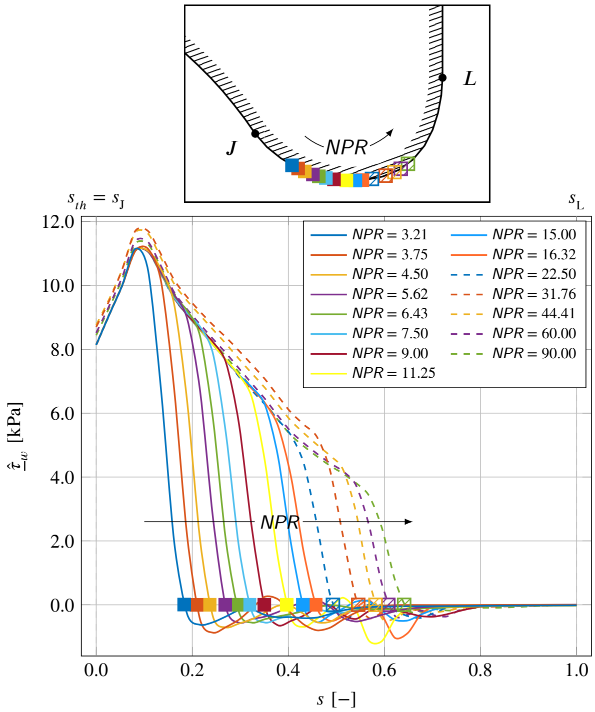

Figure 32. Wall shear stress distribution along the fillet. The squared marks highlight the location of the separation point. The upper frame highlights the region around the fillet wall.

7. Conclusions

The results presented prove that DemoP1 has a specific impulse that grows like the one of an isentropic plug nozzle. Nonetheless, featuring a lower mass flow rate due to losses related to viscosity (i.e., the boundary layer) and two-dimensional flow, it delivers less thrust. For ambient pressure values below p_{amb}^{opt}, the flow expands beyond the aerospike length, and the engine behaviour becomes equivalent to that of a bell-shaped nozzle with the same exit section area. In over-expansion conditions, though, the aerospike nozzle can achieve greater thrust and specific impulse. Because the expansion is delayed by the nozzle fillet, the spike sees a higher pressure than the one predicted by the Prandtl–Meyer theory. Within the ambient pressure range for which the reflection of the oblique shock wave located at the end of the Prandtl–Meyer expansion goes beyond the spike end, the pressure grows almost linearly after the shock itself. Downstream of point B, on the external part of the base, the pressure drops because the flow expands toward the base itself.

Over a wide range of nozzle pressure ratios, the flow separates over the spike due to SWBLI, generated by an incident shock wave. The theory presented in this work provides results that are close to those coming from the simulations. The highest errors occur at the fillet, which delivers a negative thrust contribution due to the non-pointwise expansion, and at the base due to the error in the estimation of the flow direction at the end of the spike. Despite that, the predicted thrust coefficient of the base, computed at different ambient pressure values, can be used as an upper bound evaluation. In over-expansion conditions, the base thrust oscillates with varying ambient pressures. These oscillations are related to the flow direction at the spike end. The transition nozzle pressure ratio has been estimated in the range $16.32 < NPR < 22.50$, which also contains the transition value predicted using the method proposed by Onofri in [57]. The drag due to wall shear stress reduces the thrust coefficient by about −0.75% on average, while the difference between the theoretical pressure distribution and the one obtained from the simulation is responsible for a thrust coefficient reduction of about −2.04%.

Depending on the *NPR*, the flow is able to delay the separation point over the fillet, which acts like a divergent section.

Author Contributions: Conceptualization, L.F. and N.S.; methodology, L.F.; software, L.F. and M.D.G.; validation, M.D.G. and E.S.; formal analysis, L.F.; investigation, M.D.G. and L.F.; resources, F.P.; data curation, E.S., F.R. and F.P.; writing—original draft preparation, L.F.; writing—review and editing, L.F.; visualization, L.F.; supervision, E.S., F.R. and F.P.; project administration, F.P. All authors have read and agreed to the published version of the manuscript.

Funding: This research received no external funding.

Data Availability Statement: Data is contained within the article.

Conflicts of Interest: Authors Ernesto Sozio and Federico Rossi were employed by the company Pangea Aerospace. The remaining authors declare that the research was conducted in the absence of any commercial or financial relationships that could be construed as a potential conflict of interest.

Abbreviations

The following abbreviations are used in this manuscript:

NASA	National Aeronautics and Space Administration
CEA	Chemical Equilibrium with Applications
SST	Shear Stress Transport
HLLC	Harten, Lax, van Leer, Contact
OpenFOAM	Open Field Operation And Manipulation
SSTO	Single Stage To Orbit
SWBLI	Shock Wave–Boundary Layer Interaction
DLR	Deutsches Zentrum für Luft- und Raumfahrt
NPR	Nozzle pressure ratio, -
k	Turbulent kinetic energy, m^2/s^2
ω	Specific dissipation rate, s^{-1}
p	Static pressure, Pa
p_0	Total pressure, Pa
T	Static temperature, K
T_0	Total temperature, K
C_p	Specific heat capacity at constant pressure, $J/(kg\,K)$
γ	Heat capacity ratio, -
$\mathcal{M}$	Molar mass, g/mol
ρ	Flow density, kg/m^3
c_s	Speed of sound, m/s
μ	Dynamic viscosity, $kg/(m\,s)$
Pr	Prandtl number, -
Δt	Simulation time step, s
Δt_{pp}	Post-processing time interval, s
t_a, t_b	Post-processing time interval extreme value, s
r	Radial coordinate, m
$\mathbf{x}$	Position vector, m
t	Time, s
d_e	Aerospike exit section diameter, m
d_v	Distance of the vertical farfield from the throat section, m
d_o	Distance between the outlet and the throat section, m

d_h	Distance of the horizontal farfield from the engine axis, m
r_g	Aerospike external wall radius, m
r_e	Aerospike exit section radius, m
M	Mach number, -
ξ	Mach angle, rad
$\mathcal{A}$	Effective area, m^2
A	Geometrical area, m^2
c_{sf}	Safety factor for A_{BW} area estimation, -
$\mathbf{u}$	Velocity vector, m/s
U	Velocity module, m/s
I	Turbulence intensity, -
l	Turbulence length scale, m
L	Engine length scale, m
C_μ	k-ω SST parameter, -
D_H	Hydraulic diameter m
Re_{D_H}	Reynolds number, -
Φ	Perimeter, m
l_{inf}	Distance from the boundary to the actual farfield region at which the pressure should be p_∞, m
p_{inf}	Pressure at l_{inf} distance from the boundary, Pa
u_{wave}	Advection speed, m/s
U_r	External flow speed, m/s
N_{cells}	Number of cells in the mesh, -
$\underline{t}_{exe}$	Execution time, s
$\underline{t}_{exe}$	Execution time in percentage with respect the one required by the finest mesh, -
$\underline{F}^j$	Thrust calculated from the j-th mesh, N
$\underline{e}_F$	Percentage variation in thrust compared to that calculated from the finest mesh, -
$\underline{e}_p$	Percentage variation in pressure distribution compared to that calculated from the finest mesh, -
$\Delta\dot{m}$	Mass flow rate difference with respect to the theoretical case, kg/s
$\sigma_{\dot{m}}$	Standard deviation of the mass flow rate, kg/s
C_d	Discharge coefficient, -
ϵ	Aspect ratio, -
$\dot{m}$	Mass flow rate, kg/s
R_s	Specific gas constant, J/(kg K)
C_F	Thrust coefficient, -
F	Thrust, N
$\hat{\mathbf{n}}$	Unit normal vector, -
F_j	Thrust delivered by the surface j, N
S_j	j-th surface
I	Identity matrix, -
$\boldsymbol{\tau}$	Shear stress tensor, Pa
θ	Angle between flow velocity and engine axis, rad
$\theta_{\mathrm{B}*}$	Estimated flow angle after the spike end, rad
ν	Flow direction change, rad
$\underline{\mathcal{F}}_{\mathrm{BW}}$	Averaged momentum variation through the line BW, N
δ	Wall slope, rad
$C_{F,j}$	Thrust coefficient delivered by the surface j, -
η_b	Ratio between the aerospike base radius and the exit section radius, -
$\hat{\imath}$	Unit vector parallel to the engine axis, -
$\hat{\mathbf{r}}$	Unit vector parallel to the radial direction, -
$\hat{\mathbf{t}}$	Unit vector tangent to the wall, -
τ	Wall shear stress projected along the wall, Pa

$\Delta\theta$	Angle through which a flow turns due to Prandtl–Meyer expansion, rad
cc	Combustion chamber
wss	Wall shear stress
inlet	Inlet
base	Base
th	Throat section
w	Engine wall
f	Farfield
o	Outlet
e	Engine exit section
ea	Engine axis
amb	Ambient condition
sl	Sea level
$\underline{\cdot}$	Every underlined symbol refers to a simulation result
opt	Design condition
$\hat{\cdot}$	Time average value of variable $\cdot$
$\tilde{\cdot}$	Spatial average value of variable $\cdot$

Appendix A. Mesh Convergence Analysis

A mesh convergence analysis has been performed to select a grid that allows us to achieve good results without requiring excessive computational time. The case used for this analysis features $p_{amb} = 1.013\,25 \times 10^5$ Pa. The five tested meshes are listed in Table A1: the coarsest one (A) has about 26k cells while the finest one (E) counts about 125k cells. The finer meshes have been obtained by refining the coarsest one in the region close to the spike and in the plume. Near the *outlet* and the *farfields*, the mesh is kept almost the same. Every simulation has been run with a Δt low enough to keep the maximum Courant number below 0.08. Particular attention has been paid to the steady-state results. The latter, discussed in the next sections, will be averaged between $t = 60$ ms and $t = 70$ ms, but it is too demanding to run the finest mesh simulation up to $t = 70$ ms. Therefore, the runs for the mesh convergence analysis have been stopped at $t = 48$ ms, averaging the results in the last 3 ms. The thrust reported in Figure A1 has been obtained, neglecting the wall shear stress. The error bars represent the standard deviation of the thrust evaluated between 45 ms and 48 ms. Increasing the number of cells, the thrust converges to 21.45 kN, but its standard deviation also increases a little, meaning that the results oscillate more in time. Figure A2 shows the mean value of the wall shear stress averaged over the same time range. The two coarser meshes have been discarded because the boundary layer refinement is too low to output a reliable wall shear stress value. The drag due to the wall shear stress decreases with an increase in the number of cells in the mesh.

Table A1 summarizes the mesh convergence analysis. The thrust error has been evaluated with respect to the finest mesh outcomes using the following formula:

$$\underline{e}_F^j = \frac{\underline{F}^{\mathrm{E}} - \underline{F}^j}{\underline{F}^{\mathrm{E}}}, \quad j \in [\mathrm{A}, \mathrm{B}, \mathrm{C}, \mathrm{D}, \mathrm{E}] \tag{A1}$$

where $\underline{F}^j$ is the thrust shown in Figure A1, which does not contain the wall shear stress contribution. The computational times reported in Table A1 and Figure A3 have been evaluated by running the simulations on 16 cores of a workstation with a Xeon W-3365. The choice to use 16 cores was made according to the speedup plot shown in [33] and Figure A7. In Figure A3, the solid blue line is the cubic fitting of the computational time: the cubic coefficient is quite small, but due to the huge values of x, it becomes the most dominant term. Hence, for fixed Co_{max} and a simulated time interval, the asymptotic computational complexity is $\mathcal{O}\left(N_{cells}^3\right)$. The execution time percentage, shown in Table A1, has been evaluated with respect to the most expensive simulation.

$$\underline{p}_{exe}^{j} = \frac{\underline{t}_{exe}^{\mathrm{E}} - \underline{t}_{exe}^{j}}{\underline{t}_{exe}^{\mathrm{E}}}, \quad j \in [\mathrm{A}, \mathrm{B}, \mathrm{C}, \mathrm{D}, \mathrm{E}] \tag{A2}$$

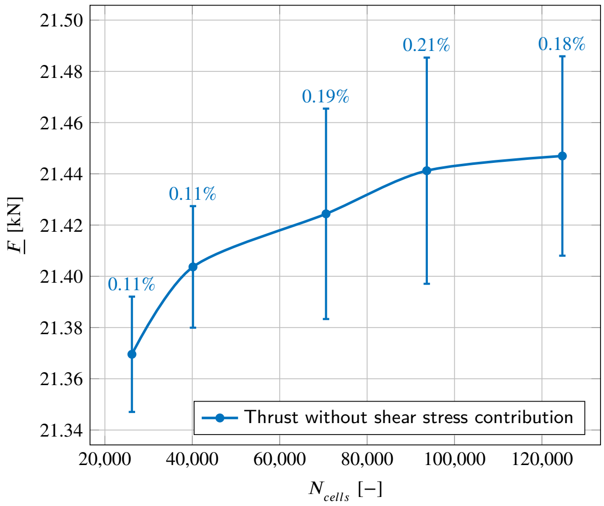

Figure A1. Average thrust calculated without shear stress using the results obtained by different meshes. The error bars represent the thrust standard deviation evaluated within 45 ms $\leq t \leq$ 48 ms. The percentage values represent the standard deviation as a percentage of the corresponding mean.

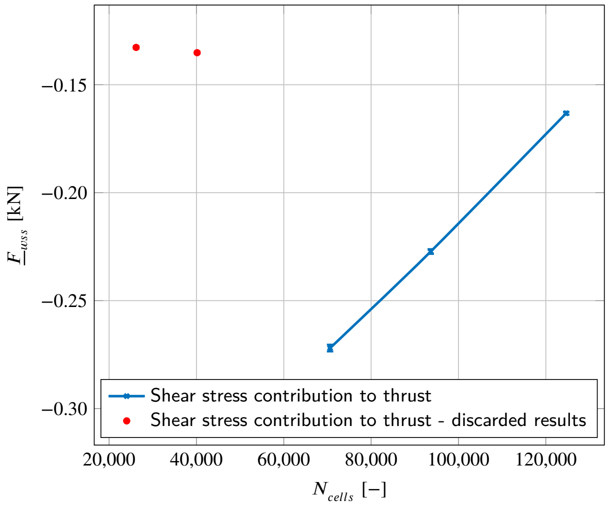

Figure A2. Average shear stress contribution to thrust. The averaging interval is 45 ms $\leq t \leq$ 48 ms.

Table A1. Results of the mesh convergence analysis. The execution time has been evaluated by running the simulations on 16 cores of a workstation with a Xeon W-3365.

Mesh	N_{cells} [−]	$\underline{t}_{exe}$ [h]	$\underline{p}_{exe}$ [%]	$\underline{F}^j$ [kN]	$\underline{e}_F$ [%]
A	26,184	34.60	7.17	21.37	0.361
B	40,157	47.92	9.92	21.40	0.202
C	70,597	116.97	24.22	21.42	0.105
D	93,651	227.49	47.11	21.44	0.027
E	124,670	482.92	100.00	21.45	0.000

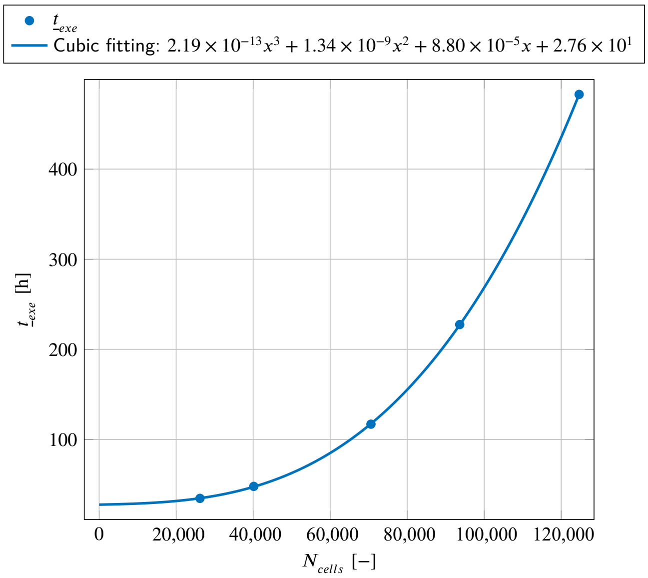

Figure A3. Simulation execution times evaluated by running the simulations on 16 cores of a workstation with a Xeon W-3365. The solid blue line is a cubic polynomial fitting.

Table A2 reports the y^+ values of the simulation with the C mesh. y^+_{min} and y^+_{max} are, respectively, the minimum and maximum values on the corresponding wall surface evaluated for $45\,\text{ms} \leq t \leq 48\,\text{ms}$, while y^+_{avg} is the average value on the corresponding surface in the same time interval. Since it holds that $y^+_{max} < 100$ for every surface, the selected wall functions can be used as boundary conditions for k and ω. Due to the mesh refinement level near the walls, the cells close to them have a size comparable to the viscous sub layer.

Table A2. Minimum, maximum, and average y^+ value on every DemoP1 surface obtained with mesh C.

Surface Name	$\underline{y}^+_{min}$	$\underline{y}^+_{max}$	$\underline{y}^+_{avg}$
Combustion chamber	1.67×10^{-4}	0.857	0.128
Converging nozzle	1.44×10^{-4}	3.66	3.06
Diverging nozzle	5.00×10^{-6}	1.79	0.398
Spike	1.31×10^{-3}	3.38	1.35
Base	4.00×10^{-6}	1.17×10^{-3}	2.93×10^{-4}
Vertical external wall	2.30×10^{-5}	2.37×10^{-4}	1.05×10^{-4}
Horizontal external wall	1.75×10^{-4}	2.41×10^{-4}	1.86×10^{-4}
External wall extension	1.79×10^{-4}	1.83×10^{-4}	1.81×10^{-4}

Figures A4 and A5 show, respectively, the pressure distribution along the spike and the absolute value of the pressure error $\underline{e}_p$ evaluated with respect to the finest mesh solution. Both figures feature the curvilinear coordinate defined in Section 4.1 on the horizontal axis of the plots.

$$\underline{e}_p = \left|\underline{p}^j - \underline{p}^{\mathrm{E}}\right|, \;\; j \in [\mathrm{A}, \mathrm{B}, \mathrm{C}, \mathrm{D}] \tag{A3}$$

The four pressure distributions obtained by meshes A, B, C, and D show similar behaviours from s_{th} up to $s = 0.75$. The errors related to meshes C and D rise and remain constant between $s = 0.75$ and the end of the spike (s_{B}). Then these pressure errors increase slightly at the DemoP1 base. The errors related to meshes A and B are lower than the ones of meshes C and D close to the end of the spike, but they increase significantly at the aerospike base.

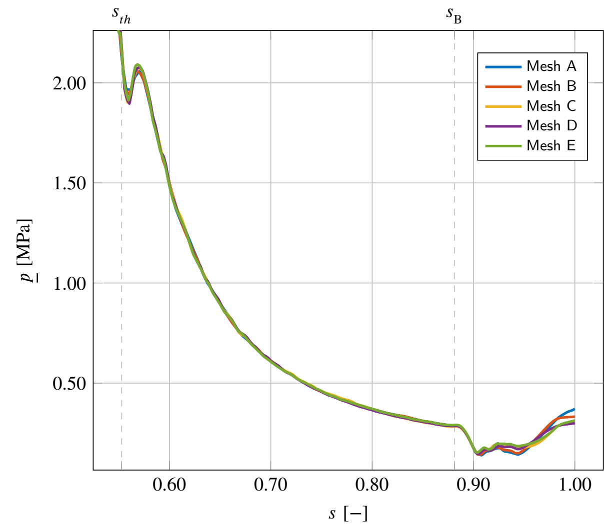

Figure A4. Pressure distribution along the spike and the base obtained using different meshes.

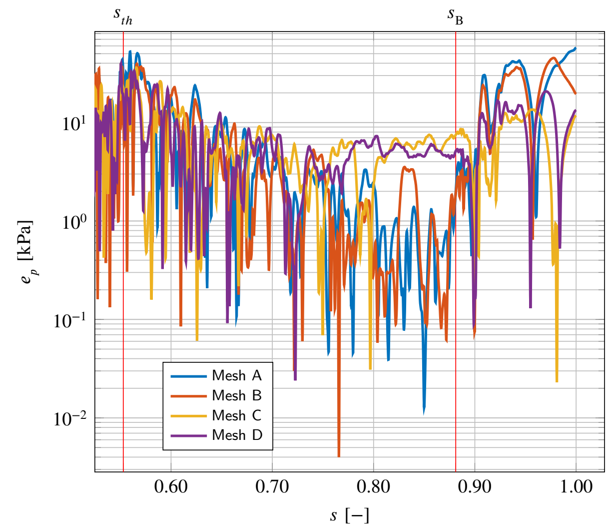

Figure A5. Pressure error obtained using different meshes. The results obtained from the associated simulation with the finest mesh are taken as the reference.

In conclusion, Figure A1 clearly shows convergence of the thrust value, but this is not the case for the wall shear stress contribution. Nevertheless, its influence is bounded between −0.27 kN and 0.0 kN. The overall uncertainty, calculated as the highest thrust variation between the three finest meshes, is about 0.13 kN, which is 0.62% of the thrust evaluated in case E. Since the execution time increases cubically with the number of cells, mesh C has been chosen as a suitable compromise between result accuracy and computational cost. In addition, this mesh also satisfies the constraint on y^+. Mesh D would be a little more accurate, but it requires too much computational time. According to the speedup shown in [33] and Figures A6 and A7, the computational time can be reduced by increasing the number of cores but entails a waste of computational power. Therefore, the employment of 16 cores has been considered a suitable compromise for the following simulations.

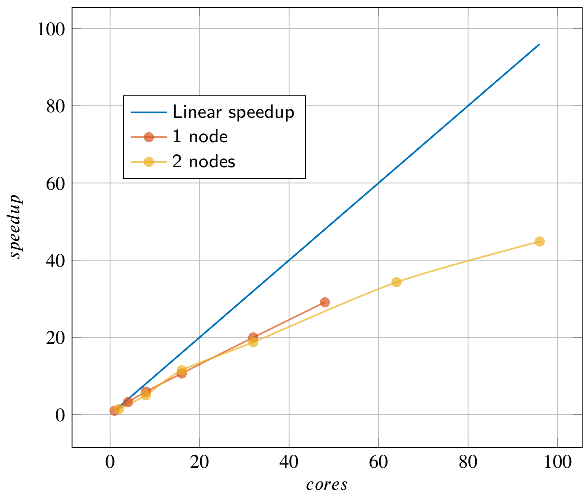

Figure A6. Simulation speedup on GALILEO 100 [63].

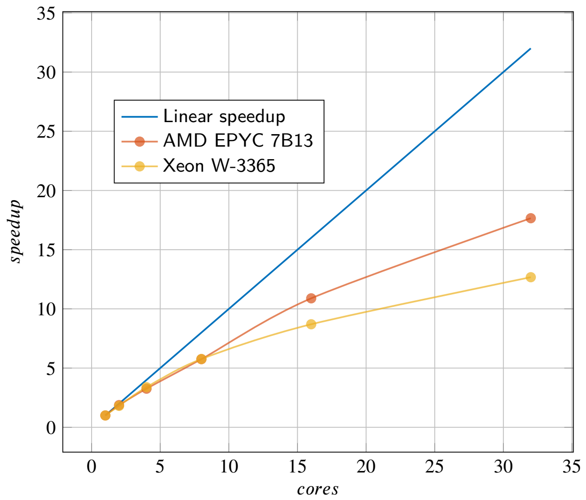

Figure A7. Simulation speedup on AMD EPYC 7B13 and Xeon W-3365.

Appendix B. Turbulent Intensity and Length Scale

Appendix B.1. Empirical Turbulence Intensity Law

The momentum balance equation on a generic cross-section straight pipe is the following:

$$(p + \Delta p)A - pA = \tau_w \, \zeta_{pipe} \, L_{pipe} \tag{A4}$$

where p is the pressure, A is the pipe cross-section area, ζ_{pipe} is the cross-section perimeter, L_{pipe} is the pipe length, and τ_w is the shear stress at the wall. This equation could be rewritten introducing the hydraulic diameter: $D_{H_{pipe}} = \frac{4A}{\zeta_{pipe}}$.

$$\Delta p \frac{A}{\zeta_{pipe}} = \tau_w \, L_{pipe} \implies \Delta p \frac{D_{H_{pipe}}}{4} = \tau_w \, L_{pipe} \tag{A5}$$

In [64] (p. 232), the friction factor for a generic pipe is defined as

$$\lambda_{pipe} = \frac{\frac{\Delta p}{L_{pipe}} D_{H_{pipe}}}{\frac{1}{2}\rho U_m^2} \tag{A6}$$

where U_m is the bulk channel velocity and ρ is the flow density. Therefore, it becomes

$$\lambda_{pipe} = 8\frac{\tau_w}{\rho U_m^2} \tag{A7}$$

and τ_w can be rewritten in terms of friction velocity u_τ.

$$\tau_w = \rho u_\tau^2 \implies \lambda_{pipe} = 8\frac{u_\tau^2}{U_m^2} \implies \frac{u_\tau}{U_m} = \sqrt{\frac{\lambda_{pipe}}{8}} \tag{A8}$$

The turbulence intensity is defined as

$$I = \frac{\sqrt{\frac{1}{3}(u' + v' + w')}}{U_m} \tag{A9}$$

where u', v', and w' are the root-mean-square velocity fluctuations along the three orthogonal directions. Close to the pipe centre, u_τ can be correlated with u', v', and w', as shown in [65] (p. 163).

$$u' = v' = w' \cong 0.8u_\tau \tag{A10}$$

Combining the previous equations,

$$I = \frac{\sqrt{\frac{1}{3}(u' + v' + w')}}{U_m} \cong 0.8\frac{u_\tau}{U_m} = 0.8\sqrt{\frac{\lambda_{pipe}}{8}} \tag{A11}$$

For the Blasius correlation [66],

$$\lambda_{pipe} \cong 0.3164\, Re_{D_H}^{-1/4} \tag{A12}$$

Therefore

$$I \cong 0.16 Re_{D_H}^{-1/8} \tag{A13}$$

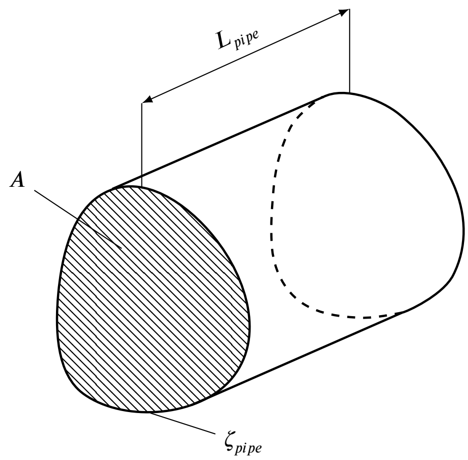

Figure A8. Sketch of pipe with generic cross-section.

Appendix B.2. Turbulence Length Scale in Pipes

The turbulent length scale in the fully developed two-dimensional pipe scenario has been evaluated according to the Nikuradses formula used in [54] (ch. 3.7.1), [67] (p. 44) and [68] (ch. 2.5):

$$\frac{l_t}{H} = 0.14 - 0.08\left(1 - \frac{y}{H}\right)^2 - 0.06\left(1 - \frac{y}{H}\right)^4 \tag{A14}$$

where l_t is the turbulence length scale, H is half of the pipe height, y is the spanwise direction coordinate, and the origin is located on one wall of the channel. The maximum value of $\frac{l_t}{H} = 0.14$ and, therefore, the maximum turbulent length scale with respect to the pipe height is $\frac{l_t}{2H} = 0.07$.

Appendix B.3. Turbulence Length Scale for Wake Flow

The turbulent scale for a wake flow is described in [54] (ch. 3.7.1) with the following equation:

$$l_t = 0.16\frac{H_{wake}}{2} = 0.08H_{wake} \tag{A15}$$

where l_t is the turbulence length scale and H_{wake} is the wake width.

Appendix C. Ideal Plug Nozzle

The ideal plug nozzle is an ideal rocket engine in which the gas expands to the ambient pressure following an isentropic expansion. Hence, its thrust coefficient at different nozzle pressure ratios can be evaluated using the isentropic nozzle theory. Differently from a bell-shaped nozzle, this engine works in optimal expansion conditions for a wide range of nozzle pressure ratios. When the $NPR \leq NPR_{opt}$, the gas reaches the ambient pressure at the engine exit section, while for $NPR > NPR_{opt}$, the gas expands beyond the engine exit section; hence the engine loses the adaptability feature, behaving like a bell-shape nozzle, with the same aspect ratio, in under-expansion conditions. The thrust coefficient can be calculated using Equation (A16).

$$C_F = \begin{cases} \sqrt{\dfrac{2\gamma^2}{\gamma-1}\left(\dfrac{2}{\gamma+1}\right)^{\frac{\gamma+1}{\gamma-1}}\left[1-\left(\dfrac{p_{amb}}{p_{0,cc}}\right)^{\frac{\gamma-1}{\gamma}}\right]} & \dfrac{p_{amb}}{p_{0,cc}} \geq \dfrac{p_{amb}^{opt}}{p_{0,cc}} \\ \sqrt{\dfrac{2\gamma^2}{\gamma-1}\left(\dfrac{2}{\gamma+1}\right)^{\frac{\gamma+1}{\gamma-1}}\left[1-\left(\dfrac{p_{amb}^{opt}}{p_{0,cc}}\right)^{\frac{\gamma-1}{\gamma}}\right]} + \left(\dfrac{p_{amb}^{opt}}{p_{0,cc}} - \dfrac{p_{amb}}{p_{0,cc}}\right)\epsilon_e & \dfrac{p_{amb}}{p_{0,cc}} < \dfrac{p_{amb}^{opt}}{p_{0,cc}} \end{cases} \tag{A16}$$

where γ is the heat capacity ratio of the gas, ϵ_e is the engine aspect ratio, p_{amb} is the ambient pressure, $p_{0,cc}$ is the total pressure in the combustion chamber, and p_{amb}^{opt} is the ambient pressure for which an equivalent bell-shape nozzle works in optimal expansion conditions. This pressure can be evaluated by solving Equation (A17) for M_e, the Mach number at the engine exit section, and then using Equation (A18).

$$\epsilon_e = \frac{1}{M_e}\sqrt{\left[\frac{1+\frac{\gamma-1}{2}M_e^2}{\frac{\gamma+1}{2}}\right]^{\frac{\gamma+1}{\gamma-1}}} \tag{A17}$$

$$\frac{p_{amb}^{opt}}{p_{0,cc}} = \left[1+\frac{\gamma-1}{2}M_e^2\right]^{\frac{\gamma}{1-\gamma}} \tag{A18}$$

The hypothesis that this engine loses the ability to adapt the expansion for ambient pressure lower than p_{amb}^{opt} is in disagreement with [5] (p. 84), in which it is supported that this engine is able to work near the optimal performance at every altitude. Nevertheless, this argument is supported by the simulation results presented in this work.

Appendix D. Flow Inclination at the End of Prandlt–Meyer Expansion

Figure A9 shows a section of an annular aerospike engine obtained using Angelino's method [40]. The spike of DemoP1 is obtained by setting $r_{\mathrm{B}} = 0\,\mathrm{m}$; then the spike is cut at 62% of the original spike length. The line JC′ represents the throat section. The angle between the velocity vector $\mathbf{u}$ and the engine axis is θ, which is positive when $\mathbf{u}$ is pointing away from the engine axis.

$$\theta = \xi - \phi \tag{A19}$$

where ϕ is the angle between the engine axis and the line JB′. It is positive when $r_{\mathrm{B}'} < r_{\mathrm{J}}$. ξ is the Mach angle:

$$\xi = \arcsin\left(\frac{1}{M}\right) \tag{A20}$$

According to [40],

$$\phi = \nu(M_e) - \nu(M) + \xi(M) \tag{A21}$$

$$\nu(M) = \sqrt{\frac{\gamma+1}{\gamma-1}}\arctan\left(\sqrt{\frac{\gamma-1}{\gamma+1}(M^2-1)}\right) - \arctan\left(\sqrt{M^2-1}\right) \tag{A22}$$

where ν is the Prandtl–Meyer function defined in Equation (A22).

$$\theta(M) = \nu(M) - \nu(M_e) \tag{A23}$$

Hence, the inclination of the flow at the end of the Prandtl–Meyer expansion is

$$\theta_{\mathrm{JB}'} = \nu(M_{\mathrm{B}'}) - \nu(M_e), \quad \frac{p^{\mathrm{B}}_{amb}}{p_{0,\mathrm{cc}}} < \frac{p_{amb}}{p_{0,\mathrm{cc}}} \leq \frac{p^{cr}_{amb}}{p_{0,\mathrm{cc}}} \tag{A24}$$

where M_e can be calculated using Equation (21), while $M_{\mathrm{B}'}$ can be obtained using Equation (A25).

$$M_{\mathrm{B}'} = \sqrt{\frac{2}{\gamma-1}\left[\left(\frac{p_{0,\mathrm{cc}}}{p_{amb}}\right)^{\frac{\gamma-1}{\gamma}} - 1\right]}, \quad \frac{p^{\mathrm{B}}_{amb}}{p_{0,\mathrm{cc}}} < \frac{p_{amb}}{p_{0,\mathrm{cc}}} \leq \frac{p^{cr}_{amb}}{p_{0,\mathrm{cc}}} \tag{A25}$$

The angle $\beta_{\mathrm{JB}'}$ is given by the following equation:

$$\beta_{\mathrm{JB}'} = \frac{\pi}{2} - \phi_{\mathrm{JB}'} = \frac{\pi}{2} - \nu(M_e) + \nu(M_{\mathrm{B}'}) - \xi(M_{\mathrm{B}'}) \tag{A26}$$

for $\frac{p^{\mathrm{B}}_{amb}}{p_{0,\mathrm{cc}}} < \frac{p_{amb}}{p_{0,\mathrm{cc}}} \leq \frac{p^{cr}_{amb}}{p_{0,\mathrm{cc}}}$. β is positive when $\hat{\mathbf{n}}$ is pointing away from the engine axis.

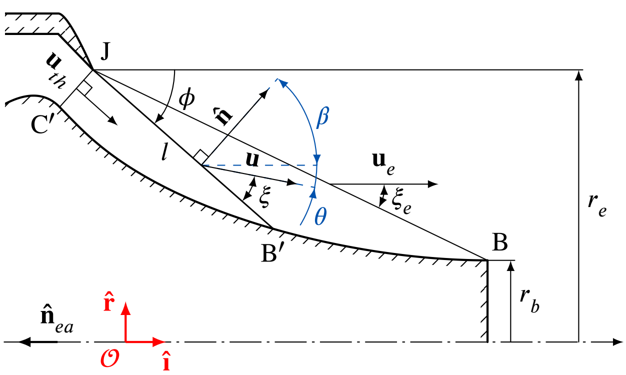

Figure A9. Annular aerospike scheme [40].

References

1. Hagemann, G.; Immich, H.; Van Nguyen, T.; Dumnov, G.E. Advanced Rocket Nozzles. *J. Propuls. Power* **1998**, *14*, 620–634. [CrossRef]
2. Sutton, G.P.; Biblarz, O. *Rocket Propulsion Elements*, 9th ed.; Wiley: Hoboken, NJ, USA, 2017.
3. Hill, P.G.; Peterson, C.R. *Mechanics and Thermodynamics of Propulsion*, 2nd ed.; Pearson: London, UK, 1992.
4. Huzel, D.K.; Huano, D.H. *Design of Liquid Propellant Rocket Engines*, 2nd ed.; Wiley: Hoboken, NJ, USA, 1967.
5. Sutton, G.P.; Biblarz, O. *Rocket Propulsion Elements*, 8th ed.; Wiley: Hoboken, NJ, USA, 2010.
6. Verma, S. Performance Characteristics of an Annular Conical Aerospike Nozzle with Freestream Effect. *J. Propuls. Power* **2009**, *25*, 783–791. [CrossRef]
7. Gayathri, N.; Senthilkumar, P.; Dineshkumar, K.; Purusothaman, M.; Sriharan, B. CFD analysis on flow through nozzle of conical type and truncated conical plug type. *Mater. Today Proc.* **2023**, *72*, 2387–2394. [CrossRef]
8. Nair, P.P.; Suryan, A.; Kim, H.D. Computational study on flow through truncated conical plug nozzle with base bleed. *Propuls. Power Res.* **2019**, *8*, 108–120. [CrossRef]
9. Liu, X.Y.; Cheng, M.; Zhang, Y.Z.; Wang, J.P. Design and optimization of aerospike nozzle for rotating detonation engine. *Aerosp. Sci. Technol.* **2022**, *120*, 107300. [CrossRef]
10. Wang, C.H.; Liu, Y.; Qin, L.Z. Aerospike nozzle contour design and its performance validation. *Acta Astronaut.* **2009**, *64*, 1264–1275. [CrossRef]
11. Wang, Y.; Lin, Y.; Eri, Q.; Kong, B. Flow and thrust characteristics of an expansion–deflection dual-bell nozzle. *Aerosp. Sci. Technol.* **2022**, *123*, 107464. [CrossRef]
12. Wang, Y.; Eri, Q.; Huang, J.; Kong, B. Multi-objective aerodynamic optimization of expansion–deflection nozzle based on B-spline curves. *Aerosp. Sci. Technol.* **2024**, *147*, 109016. [CrossRef]
13. Li, R.; Xu, J.; Lv, H.; Lv, D.; Song, J. Numerical investigations of the nozzle performance for a rocket-based rotating detonation engine with film cooling. *Aerosp. Sci. Technol.* **2023**, *136*, 108221. [CrossRef]
14. Huang, Y.; Xia, H.; Chen, X.; Luan, Z.; You, Y. Shock dynamics and expansion characteristics of an aerospike nozzle and its interaction with the rotating detonation combustor. *Aerosp. Sci. Technol.* **2021**, *117*, 106969. [CrossRef]
15. Lv, H.; Xu, J.; Li, R.; Zhou, J.; Yu, K. Numerical investigations of different liner lengths of axial film cooling for a rotating detonation engine. *Aerosp. Sci. Technol.* **2024**, *149*, 109172. [CrossRef]
16. Li, R.; Xu, J.; Lv, H.; Yu, K.; Zhou, J. Numerical investigations of the nozzle performance of a rotating detonation engine with axially adjustable cowl and spike. *Aerosp. Sci. Technol.* **2025**, *158*, 109878. [CrossRef]
17. Zhu, Y.; Wang, K.; Wang, Z.; Zhao, M.; Jiao, Z.; Wang, Y.; Fan, W. Study on the performance of a rotating detonation chamber with different aerospike nozzles. *Aerosp. Sci. Technol.* **2020**, *107*, 106338. [CrossRef]
18. Ma, J.Z.; Bao, W.; Wang, J.P. Experimental research of the performance and pressure gain in continuous detonation engines with aerospike nozzles. *Aerosp. Sci. Technol.* **2023**, *140*, 108464. [CrossRef]
19. Shen, D.; Ma, J.Z.; Sheng, Z.; Rong, G.; Wu, K.; Zhang, Y.; Wang, J. Spinning pulsed detonation in rotating detonation engine. *Aerosp. Sci. Technol.* **2022**, *126*, 107661. [CrossRef]
20. Bell, K.; Schwer, D.; Agrawal, A.K. Profiling cross-sectional area of a radial rotating detonation combustor to increase pressure gain. *Aerosp. Sci. Technol.* **2023**, *133*, 108096. [CrossRef]
21. Tian, H.; Guo, Z.; Hao, Z.; Hedong, L.; Li, C. Numerical and experimental investigation of throttleable hybrid rocket motor with aerospike nozzle. *Aerosp. Sci. Technol.* **2020**, *106*, 105983. [CrossRef]
22. Geron, M.; Paciorri, R.; Nasuti, F.; Sabetta, F. Flowfield analysis of a linear clustered plug nozzle with round-to-square modules. *Aerosp. Sci. Technol.* **2007**, *11*, 110–118. [CrossRef]
23. Liu, Y.; Liu, R.; Yang, W.; Yang, H.; Wang, H.; Zhao, C.; Xv, C. Numerical investigation of thrust vector performance and flow separation in clustered annular aerospike nozzles with differential throttling. *Aerosp. Sci. Technol.* **2026**, *168*, 110919. [CrossRef]
24. Schwarzer-Fischer, E.; Abel, J.; Sieder-Katzmann, J.; Propst, M.; Bach, C.; Scheithauer, U.; Michaelis, A. Study on CerAMfacturing of Novel Alumina Aerospike Nozzles by Lithography-Based Ceramic Vat Photopolymerization (CerAM VPP). *Materials* **2022**, *15*, 3279. [CrossRef]
25. Pangea Aerospace, 2023. Available online: https://www.pangeapropulsion.com/en/ (accessed on 15 December 2025).
26. Rossi, F.; Esnault, G.; Sápi, Z.; Palumbo, N.; Argemi, A.; Bergström, R. Research Activities in the Development of DemoP1: A LOX/LNG Aerospike Engine Demonstrator. In Proceedings of the 7th Edition of the Space Propulsion Conference, Virtual, 17–19 March 2021.
27. Rossi, F.; Sápi, Z.; Palumbo, N.; Demediuk, A.; Ampudia, M. Manufacturing and Hot-Fire Test Campaign of the DemoP1 Aerospike Engine Demonstrator. In Proceedings of the 8th Edition of the Space Propulsion Conference, Estroil, Portugal, 9–13 May 2022.
28. Aenium Engineering—High Performance Additive Manufacturing. 2023. Available online: https://aenium.es/ (accessed on 15 December 2025).

29. Argemí, A. Flight of the aerospike. *Met. Powder Rep.* **2021**, *76*, 12–15. [CrossRef]
30. Fadigati, L.; Rossi, F.; Souhair, N.; Ravaglioli, V.; Ponti, F. Development and simulation of a 3D printed liquid oxygen/liquid natural gas aerospike. *Acta Astronaut.* **2024**, *216*, 105–119. [CrossRef]
31. Fadigati, L. Numerical Simulation of the Flow and Performance Evaluation of an Aerospike Engine. Ph.D. Thesis, University of Bologna, Bologna, Italy, 2024.
32. Gagliardi, M.D.; Fadigati, L.; Souhair, N.; Ponti, F. Validation of a numerical strategy to simulate the expansion around a plug nozzle. In *Materials Research Proceedings*; MRF: Padova, Italy, 2023; Volume 37, pp. 695–698. [CrossRef]
33. Fadigati, L.; Sozio, E.; Rossi, F.; Souhair, N.; Ponti, F. Advanced aerodynamic analysis of the supersonic flow field of an aerospike engine. *Aerosp. Sci. Technol.* **2025**, *158*, 109908. [CrossRef]
34. Toro, E.F. The HLLC Riemann solver. *Shock Waves* **2019**, *29*, 1065–1082. [CrossRef]
35. Menter, F.R. Two-equation eddy-viscosity turbulence models for engineering applications. *AIAA J.* **1994**, *32*, 1598–1605. [CrossRef]
36. Menter, F.R.; Kuntz, M.; Langtry, R. Ten Years of Industrial Experience with the SST Turbulence Model. In Proceedings of the Turbulence, Heat, and Mass Transfer, Antalya, Turkey, 12–17 October 2003; pp. 625–632.
37. Gordon, S.; McBride, B.J. *Computer Program for Calculation of Complex Chemical Equilibrium Compositions and Applications I. Analysis*; NASA Reference Publication; NASA: Washington, DC, USA, 1994.
38. McBride, B.J.; Gordon, S. *Computer Program for Calculation of Complex Chemical Equilibrium Compositions and Applications II. Users Manual and Program Description*; NASA Reference Publication; NASA: Washington, DC, USA, 1996.
39. Bonnie, J.M.; Gordon, S. *Lewis Research Center Cleveland, Ohio*; NASA Reference Publication; NASA: Washington, DC, USA, 1992.
40. Angelino, G. Approximate method for plug nozzle design. *AIAA J.* **1964**, *2*, 1834–1835. [CrossRef]
41. EOS M 290-Mid-Size 3D Printing. 2023. Available online: https://www.eos.info/it?utm_source=google&utm_medium=cpc&utm_campaign=brand_emea&utm_term=eos%203d&utm_campaign=%5Bwyn%5D+Brand+%5BIT%5D+%5BS%5D&utm_source=adwords&utm_medium=ppc&hsa_acc=3851378066&hsa_cam=22294787911&hsa_grp=172971710822&hsa_ad=735217097744&hsa_src=g&hsa_tgt=kwd-390601728&hsa_kw=eos%203d&hsa_mt=p&hsa_net=adwords&hsa_ver=3&gad_source=1&gad_campaignid=22294787911&gclid=EAIaIQobChMIxYSy4PjGkQMVb62DBx0L9iZhEAAYASAAEgI6XPD_BwE (accessed on 15 December 2025).
42. Cooper, K.G.; Lydon, J.L.; LeCorre, M.D.; Jones, Z.C.; Scannapieco, D.S.; Ellis, D.L.; Lerch, B.A. *Three-Dimensional Printing GRCop-42*; Technical Report; NASA: Washington, DC, USA, 2018.
43. Gradl, P.R.; Greene, S.E.; Protz, C.; Bullard, B.; Buzzell, J.; Garcia, C.; Wood, J.; Osborne, R.; Hulka, J.; Cooper, K.G. Additive Manufacturing of Liquid Rocket Engine Combustion Devices: A Summary of Process Developments and Hot-Fire Testing Results. In Proceedings of the 2018 Joint Propulsion Conference, Cincinnati, OH, USA, 9–11 July 2018. [CrossRef]
44. Soman, S.; Suryan, A.; Nair, P.P.; Dong Kim, H. Numerical Analysis of Flowfield in Linear Plug Nozzle with Base Bleed. *J. Spacecr. Rocket.* **2021**, *58*, 1786–1798. [CrossRef]
45. Zang, B.; Vevek, U.S.; Tze How, D.N. OpenFOAM based numerical simulation study of an underexpanded supersonic jet. In Proceedings of the 55th AIAA Aerospace Sciences Meeting, Grapevine, TX, USA, 9–13 January 2017; American Institute of Aeronautics and Astronautics: Reston, VA, USA, 2017. [CrossRef]
46. Jency, A.; Bajpai, A.; Appar, A.; Kumar, R. Comparative analysis of flow field and thrust behaviour of plug nozzles in continuum vs. rarefied conditions. *Aerosp. Sci. Technol.* **2025**, *157*, 109821. [CrossRef]
47. Wilcox, D. *Turbulence Modeling for CFD*, 3rd ed.; Hardcover; DCW Industries: La Canada, CA, USA, 2006.
48. Finlayson, M.A. ANSYS Fluent User's Guide, 2022 R1. 2022. Available online: https://ansyshelp.ansys.com/public//Views/Secured/corp/v252/en/flu_ug/flu_ug.html (accessed on 15 December 2025).
49. Wilcox, D.C. Reassessment of the scale-determining equation for advanced turbulence models. *AIAA J.* **1988**, *26*, 1299–1310. [CrossRef]
50. OpenFOAM: User Guide: OmegaWallFunction. 2021. Available online: https://www.openfoam.com/documentation/guides/latest/doc/guide-bcs-wall-turbulence-omegaWallFunction.html (accessed on 15 December 2025).
51. Poinsot, T.J.; Lelef, S.K. Boundary conditions for direct simulations of compressible viscous flows. *J. Comput. Phys.* **1992**, *101*, 104–129. [CrossRef]
52. Iurashev, D.; Campa, G.; Anisimov, V.V.; Cosatto, E. Two-step approach for pressure oscillations prediction in gas turbine combustion chambers. *Int. J. Spray Combust. Dyn.* **2017**, *9*, 424–437. [CrossRef]
53. Lucchese, L. Implementation of non-reflecting boundary conditions in OpenFOAM. In *CFD with OpenSource Software*; Chalmers University: Gothenburg, Sweden, 2022.
54. Versteeg, H.K.; Malalasekera, W. *An Introduction to Computational Fluid Dynamics: The Finite Volume Method*, 2nd ed.; Pearson/Prentice Hall: Harlow, UK, 2007.
55. George, E. Prandtl-Meyer Flow and Shock-Expansion Theory. In *Gasdynamics—Theory and Applications*; American Institute of Aeronautics and Astronautics: Reston, VA, USA, 1986.

56. Nasuti, F.; Onofri, M. Theoretical Analysis and Engineering Modeling of Flowfields in Clustered Module Plug Nozzles. *J. Propuls. Power* **1999**, *15*, 544–551. [CrossRef]
57. Onofri, M.; Calabro, M.; Hagemann, G.; Immich, H.; Sacher, P.; Nasuti, F.; Reijasse, P. Plug nozzles: Summary of flow features and engine performance-Overview of RTO/AVT WG 10 subgroup 1. In Proceedings of the 40th AIAA Aerospace Sciences Meeting & Exhibit, Aerospace Sciences Meetings, Reno, NV, USA, 14–17 January 2002; American Institute of Aeronautics and Astronautics: Reston, VA, USA, 2002. [CrossRef]
58. Cardenas, I.R.; Laín, S.; Lopez, O.D. A Review of Aerospike Nozzles: Current Trends in Aerospace Applications. *Aerospace* **2025**, *12*, 519. [CrossRef]
59. Chutkey, K.; Vasudevan, B.; Balakrishnan, N. Analysis of Annular Plug Nozzle Flowfield. *J. Spacecr. Rocket.* **2014**, *51*, 478–490. [CrossRef]
60. Chang, P.K. *Separation of Flow*; Pergamon: Oxford, UK, 1970.
61. Herrin, J.L.; Dutton, J.C. Supersonic base flow experiments in the near wake of a cylindrical afterbody. *AIAA J.* **1994**, *32*, 77–83. [CrossRef]
62. Fick, M.; Schmucker, R.H. Performance aspects of plug cluster nozzles. *J. Spacecr. Rocket.* **1996**, *33*, 507–512. [CrossRef]
63. Galileo100. 2023. Available online: https://www.hpc.cineca.it/systems/hardware/galileo100/ (accessed on 15 December 2025).
64. De Lemos, M.J. Applications in Hybrid Media. In *Turbulence in Porous Media*; Elsevier: Amsterdam, The Netherlands, 2012; pp. 199–352. [CrossRef]
65. Tennekes, H.; Lumley, J.L. *A First Course in Turbulence*; The Mit Press: Cambridge, MA, USA, 1972.
66. Blasius, H. Das Aehnlichkeitsgesetz bei Reibungsvorgängen in Flüssigkeiten. In *Mitteilungen über Forschungsarbeiten auf dem Gebiete des Ingenieurwesens*; Springer: Berlin/Heidelberg, Germany, 1913; pp. 1–41. [CrossRef]
67. Nikuradse, J. *Laws of Flow in Rough Pipes* ; National Advisory Committee for Aeronautics (NACA): Washington, DC, USA, 1950.
68. Antonialli, L.A.; Silveira-Neto, A. Theoretical Study of Fully Developed Turbulent Flow in a Channel, Using Prandtl's Mixing Length Model. *J. Appl. Math. Phys.* **2018**, *6*, 677–692. [CrossRef]